HHS Public Access

Author manuscript

Cell Rep. Author manuscript; available in PMC 2019 July 11.

Published in final edited form as:

Cell Rep. 2019 May 14; 27(7): 2171–2183.e5. doi:10.1016/j.celrep.2019.04.065.

Partial Cone Loss Triggers Synapse-Specific Remodeling and Spatial Receptive Field Rearrangements in a Mature Retinal Circuit

Rachel A. Care[1], **David B. Kastner**[2], **Irina De la Huerta**[3,9], **Simon Pan**[1,9], **Atrey Khoche**[4], **Luca Della Santina**[5], **Clare Gamlin**[6,10], **Chad Santo Tomas**[7], **Jenita Ngo**[5], **Allen Chen**[8], **Yien-Ming Kuo**[5], **Yvonne Ou**[5], and **Felice A. Dunn**[5,11,*]

[1]Graduate Program in Neuroscience, University of California, San Francisco, San Francisco, CA 94158, USA

[2]Department of Psychiatry, University of California, San Francisco, San Francisco, CA 94143, USA

[3]Department of Ophthalmology and Visual Sciences, Vanderbilt University Medical Center, Nashville, TN 37232, USA

[4]Department of Bioengineering, University of California, Berkeley, Berkeley, CA 94720, USA

[5]Department of Ophthalmology, University of California, San Francisco, San Francisco, CA 94143, USA

[6]Program in Neuroscience, Department of Biological Structure, University of Washington, Seattle, WA 98195, USA

[7]Department of Molecular, Cell and Developmental Biology, University of California, Santa Cruz, Santa Cruz, CA 95064, USA

[8]Department of Neuroscience, University of Rochester, Rochester, NY 14627, USA

[9]These authors contributed equally

[10]Present address: Allen Institutes for Brain Science, Seattle, WA 98109, USA

[11]Lead Contact

SUMMARY

*Correspondence: felice.dunn@ucsf.edu.

AUTHOR CONTRIBUTIONS

Conceptualization, R.A.C., D.B.K., I.D.l.H., and F.A.D.; Methodology, R.A.C., D.B.K., I.D.l.H., S.P., L.D.S., C.G., Y.M.K., and F.A.D.; Software, R.A.C., D.B.K., L.D.S., and F.A.D.; Validation, A.K. and A.C.; Formal Analysis, R.A.C., D.B.K., I.D.l.H., S.P., C.S.T., A.K., J.N., A.C., and F.A.D.; Investigation, R.A.C., I.D.l.H., S.P., L.D.S., and F.A.D.; Resources, Y.O. and Y.M.K.; Data Curation, L.D.S.; Writing – Original Draft, R.A.C., I.D.l.H., S.P., and F.A.D.; Writing – Review and Editing, R.A.C. and F.A.D.; Visualization, R.A.C., D.B.K., L.D.S., and F.A.D.; Supervision, R.A.C. and F.A.D.; Project Administration, R.A.C. and F.A.D.; Funding Acquisition, R.A.C. and F.A.D.

SUPPLEMENTAL INFORMATION

Supplemental Information can be found online at https://doi.org/10.1016/j.celrep.2019.04.065.

DECLARATION OF INTERESTS

The authors declare no competing interests.

Resilience of neural circuits has been observed in the persistence of function despite neuronal loss. In vision, acuity and sensitivity can be retained after 50% loss of cones. While neurons in the cortex can remodel after input loss, the contributions of cell-type-specific circuits to resilience are unknown. Here, we study the effects of partial cone loss in mature mouse retina where cell types and connections are known. At first-order synapses, bipolar cell dendrites remodel and synaptic proteins diminish at sites of input loss. Sites of remaining inputs preserve synaptic proteins. Second-order synapses between bipolar and ganglion cells remain stable. Functionally, ganglion cell spatio-temporal receptive fields retain center-surround structure following partial cone loss. We find evidence for slower temporal filters and expanded receptive field surrounds, derived mainly from inhibitory inputs. Surround expansion is absent in partially stimulated control retina. Results demonstrate functional resilience to input loss beyond pre-existing mechanisms in control retina.

Graphical Abstract

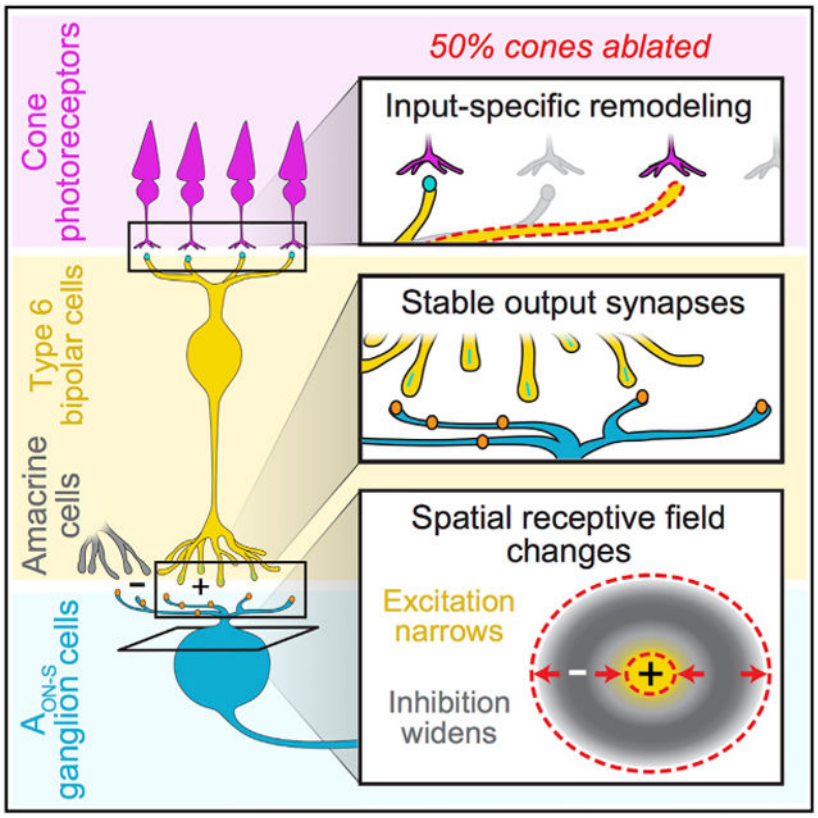

In Brief

Care et al. find that photoreceptor ablation causes structural rearrangement of bipolar cell input synapses while output synapses endure. Functionally, recipient ganglion cells show altered receptive field sizes, an effect not seen after partial stimulation of control retina, demonstrating *de novo* changes that occur in inhibitory circuitry after photoreceptor loss.

INTRODUCTION

Loss of neuronal input can occur in injury, degenerative disease, and aging. The consequences of such loss are often not functionally perceived. For example, it has been estimated that Parkinson's patients can lose 70% of dopaminergic neurons before showing clinical signs (Naoi and Maruyama, 1999). Similarly, live imaging of cone photoreceptors in human retina coupled with psychophysical examination suggests that visual acuity and sensitivity are minimally compromised even following loss of 50% of the cone population (Ratnam et al., 2013). It is unclear what contributes to behavioral resilience to input loss. Either or both of the following possibilities could contribute: the sensory circuit has pre-existing mechanisms, e.g., highly overlapping circuits or adaptation, built in to withstand partial input loss and/or has *de novo* mechanisms that react to input loss (Keck et al., 2008, 2011, 2013). Distinguishing between these possibilities requires a system with access to well-defined sensory circuits and precise control over input loss.

Such a well-defined circuit can be found in the CNS's retina, where specific types of photoreceptors, bipolar cells, and ganglion cells connect in sequence. In the retina, previous models of photoreceptor disease consist of genetic insults that disrupt function during development or physical ablation that destroys spatially contiguous populations of photoreceptors (Strettoi et al., 2002, 2003; Haverkamp et al., 2006; Sher et al., 2013; Vessey et al., 2014). However, in diseases such as age-related macular degeneration, photoreceptor cell loss often starts during adulthood and is initially sparse (Zayit-Soudry et al., 2013).

Here, we use transgenic mouse lines that selectively express the diphtheria toxin (DT) receptor (DTR) in cones, allowing for temporal control of ablation mediated by DT. We ablated subsets of cones, allowing us to assess the retina's potential for modifying existing synapses and/or making new synapses with the remaining cones. We then examined the effects of this limited cone loss on the morphology of well-characterized connections from the cones to the type 6 ON cone bipolar cells to their major postsynaptic partners, the alpha ON-sustained ganglion cells ($A_{ON\text{-}S}$). At the level of bipolar cells, we examined input (first-order) and output (second-order) synapses to identify sites of resilience to cone loss. At the level of ganglion cells, we examined morphological and functional resilience. We find that type 6 bipolar cell dendrites remodel following cone death in mature retina; however, the number of output synapses in the bipolar cell is invariant to input loss. Despite this structural stability, we uncovered functional changes in ganglion cell spatio-temporal receptive fields. With diminished cone inputs, $A_{ON\text{-}S}$ exhibit slower temporal filters and wider receptive field surrounds. Changes to the spatial receptive field are distinct from partial stimulation of control retina, suggesting *de novo* changes within the retinal circuit following cone loss. This study provides the evidence for resilience within mature retina that could explain the lack of functional deficit associated with partial cone loss.

RESULTS

Selective Ablation of Majority of Cones in Adult Mouse Retina within 3 Days

To ablate the presynaptic cone population after development of the retina, we injected DT intramuscularly at post-natal day 30 (P30) in DT receptor (DTR)-positive and DTR-negative

control animals (Figure 1A). We observed retinas at 3 to 60 days following DT injection (Figure 1B). Cone death was complete within 3 days and no further cone loss was observed up to 60 days after DT injection (Figure S1F). This rapid reduction in cone density is consistent with the mechanism of DT, which initiates apoptosis within 3 days (Buch et al., 2005). We used two mouse lines throughout our study: the *OPN1SW-Cre* line expresses Cre-recombinase under the S-opsin promoter and the *OPN1MW-Cre* line expresses Cre-recombinase under the M-opsin promoter (Akimoto et al., 2004; Le et al., 2004). Because most mouse cones co-express both S- and M-opsin (Applebury et al., 2000), both Cre lines target a large population of cones that express both S- and M-opsin (Figures S1A–S1E). Variability in efficacy of injection and expression of DTR caused a range of cone loss (Figures 1C and 1D). Throughout the study, we found no significant differences between results from the *OPN1SW-Cre* × *DTR* and *OPN1MW-Cre* × *DTR* lines, and so we have combined the results and refer to them as *DTR*. Despite the dorsal-ventral gradient of S- and M-opsin expression in the mouse retina, we found no significant difference in surviving cone density between dorsal and ventral regions after DT injection (dorsal: 5,320 ± 3,080, n = 14; ventral: 5,199 ± 2,592 cones/mm^2, n = 42; median ± interquartile range [IQR], p = 0.36, rank sum). The cone densities in control animals are comparable to previous reports of mouse cone density (Jeon et al., 1998).

To determine whether other retinal cell types were affected by DT injection, we quantified populations of retinal cells. We found no reduction in the rod population after partial cone loss (Figures S1I and S1Q–S1T). We also found no reduction in the amacrine and bipolar cell populations in the inner nuclear layer (Figure S1T), nor in populations of horizontal cells, ganglion cells, microglia, and Müller glia (Figure S2; Table S1). Partial cone loss did not activate microglia or Müller glia as determined by absence of the protein cluster of differentiation 68 (CD68) and glial fibrillary acidic protein (GFAP) (data not shown). Together, these results demonstrate that our DT system eliminates a majority of cones regardless of their opsin expression within 3 days after toxin injection, while sparing other retinal cell types. We leveraged this system to examine structural and functional changes in a well-defined microcircuit following acute cone loss.

First-Order Synapse: Type 6 Cone Bipolar Cell Dendrites Do Not Require a Cone for Stability

Previous work provides evidence that developing postsynaptic dendrites sprout in the absence of the dominant presynaptic partner (Haverkamp et al., 2006; Michalakis et al., 2013). To examine the impact of presynaptic partner loss on postsynaptic dendritic morphology in the mature retina, we measured the number of primary dendrites and cone contacts in bipolar cells. We took advantage of the type 6 bipolar cell's stereotyped morphology and simple connectivity pattern of receiving input from the four nearest cones, regardless of opsin expression (Dunn and Wong, 2012). Isolated type 6 bipolar cells were visualized in the *Grm6-TdTomato* line (Kerschensteiner et al., 2009). After determining that bipolar cells were unaffected by DT injection (Figure S1), we were able to identify type 6 bipolar cells in control and DTR retina by their axon terminals, which co-localize with the innermost band of synaptotagmin-2 (Syt2) labeling (Figure 2A; Wässle et al., 2009).

We imaged type 6 bipolar cell dendrites (Figure 2B) and the cones within their dendritic fields (Figures 2C and 2D). No differences were observed between the shortest and longest time points, so the data were pooled (number of primary dendrites in DTR retina for 5 days versus 60 days: 3.0 ± 2.0 versus 3.0 ± 1.5 dendrites, median ± IQR, p = 0.46, rank sum; length of primary dendrites in DTR retina for 5 days versus 60 days: 10.03 ± 5.13 versus 10.34 ± 5.35 μm, median ± IQR, p = 0.89, rank sum). We identified synaptic contact between bipolar cell dendrites and cones by volume overlap (Figures 2D and 2E). While type 6 bipolar cells in control retina had 4 ± 1 cone contacts (n = 44 bipolar cells), after cone loss, type 6 bipolar cell dendrites in DTR retina had 2 ± 1 cone contacts (n = 76 bipolar cells) (median ± IQR, p = 2.78e-10, rank sum). This reduction in cone contacts by half is in accordance with the cone death we induced, and suggests that most type 6 bipolar cells do not make new cone contacts to replace those lost.

To understand how dendrites respond to loss of cone contacts, we counted the number of dendrites per type 6 (Figure 2F). Dendrites at least 1 μm long off the soma were considered primary dendrites. After cone loss, the number of primary dendrites was maintained (control, 3 ± 1, n = 44; DTR, 3 ± 2 primary dendrites, n = 76; median ± IQR, p = 0.99, rank sum), despite the decrease in cone contacts. Representative images of dendrites remaining without cone contacts are shown in Figures 2B–2D, and dendrites without cone contacts were present even 60 days after cone loss (not shown). These data indicate that cone input is not required for a dendrite to persist.

First-Order Synapse: Remaining Type 6 Cone Bipolar Dendrites Extend and Lose Terminal Morphology

While dendrites in the developing retina exhibit remodeling after input loss, no reports have been made of remodeling in mature cone bipolar cells. To determine how dendrite morphology was influenced by cone loss in adulthood, we quantified the presence of specialized dendritic terminals, the length of primary dendrites, and dendritic complexity.

Most type 6 bipolar cell dendrites in control retina contact cones via specialized terminals, i.e., claws. The number of claws per bipolar cell was significantly less in DTR retina compared to control retina (Figure 2G; control, 3 ± 1; DTR, 2 ± 1 claws; median ± IQR, p = 2.73e-9, rank sum). These results suggest that claw loss follows cone loss and is evidence of remodeling. The diameters of remaining claws were not different from control, which indicates that remaining claws do not expand their synaptic contact area (control, 3.3 ± 4.2; DTR, 2.7 ± 4.9 μm; median ± IQR, p = 0.56, rank sum). The next indicator of remodeling was primary dendritic length. In DTR retina, dendrite lengths extended significantly beyond those from control retina (Figure 2H; control, 8.7 ± 8.0, n = 166 dendrites; DTR, 11.4 ± 5.2μm, n = 232 dendrites; median ± IQR, p = 9.5e-8, rank sum). The longest branch lengths were associated with branches terminating in cone contacts. Such results suggest that either new contacts were made with cones outside of the bipolar cell's original dendritic field or that dendrites with existing cone contacts extended to follow cones that may have translocated in the sparser cone mosaic.

From each primary dendrite, we quantified the branches of secondary order or greater, excluding those within a claw. We found no significant difference in branching patterns

(Figure 2I; control, 0 ± 1; DTR, 1 ± 2 branches; median ± IQR, p = 0.94, rank sum). Similarly, we found no change in the dendritic territories (Figure 2J; control, 113.9 ± 69; DTR, 137.5 ± 97 μm^2; median ± IQR, p = 0.95, rank sum). Such results suggest that the complexity and area of bipolar cell dendritic branches is maintained in the face of cone loss.

Across our morphological measurements, we find that type 6 bipolar cells remodel dendrites to dismantle terminal specializations that have lost cone partners while extending primary dendrites, potentially in search of new synaptic cone partners. Taken together, these results show that type 6 cone bipolar cells in the mature retina are capable of remodeling, but that within 60 days, this remodeling does not compensate for the number of lost cone inputs.

First-Order Synapse: Postsynaptic Glutamate Receptors Are Localized to Cone Contacts after Partial Cone Loss

To understand whether these remodeled bipolar cell dendrites contain the appropriate synaptic machinery for functional connectivity, we next investigated how the glutamate receptor localization changes in these type 6 bipolar cells following cone ablation. We immunostained for the postsynaptic metabotropic glutamate receptor 6 (mGluR6) and measured fluorescence intensity along line segments that followed primary dendrites from the dendritic base (next to soma) to tip (Figures 3A, lines, and 3B). We normalized this distance and plotted the location of the peak mGluR6 fluorescence to compare across cells (Figure 3C). For both control and DTR conditions with cone contacts, peak mGluR6 fluorescence was found in the distal quarter of the dendrite, toward the synapse (Figures 3B and 3C, top, middle; control with cone, 0.82 ± 0.19, n = 100 dendrites; DTR with cone, 0.89 ± 0.29, n = 73 dendrites; median ± IQR, p = 0.49, rank sum). In the DTR condition without a cone contact, mGluR6 localization was variable and significantly different from DTR branches with a cone contact (Figures 3B and 3C, bottom; DTR without cone, 0.51 ± 0.57 μm, n = 82 dendrites; median ± IQR, p = 6.18e-7, rank sum) and from control branches with a cone contact (p = 5.63e-9, rank sum). This demonstrates that the presence of the cone stabilizes the mGluR6 protein to the bipolar cell dendritic terminals; in the absence of a cone, the mGluR6 becomes mislocalized. Within a single bipolar cell, dendritic branches exhibited cone-dependent mGluR6 distributions, indicating that mGluR6 localization is regulated in a branch-specific manner. This mislocalization is consistent with our previous findings (Dunn, 2015) and indicates that these mGluR6 rearrangements are stable for 60 days after cone loss. In addition to mGluR6, the transduction channel Trpm1 also colocalized with mGluR6, such that both proteins are either present with a cone or absent without a cone (Figure S3).

Second-Order Synapse: Bipolar Cell Output Synapses and Major Ganglion Cell Partners Remain Morphologically Stable

Previous work demonstrates that the dendritic inputs and axonal outputs of bipolar cells are coordinated in their growth during development (Soto et al., 2012; Johnson et al., 2017). Given the rearrangements we observed in the bipolar cell inputs, we next aimed to understand whether there were corresponding changes in their output. For a subset of the type 6 bipolar cells whose dendrites we had analyzed, we measured the area of their axon territory and found no significant differences between type 6 bipolar cells in control and

DTR retina (control, 181 ± 48.1, n = 19 bipolar cells; DTR, 232 ± 106.5 μm^2, n = 23 bipolar cells; median ± IQR; p = 0.06, rank sum; data not shown). These findings indicate that type 6 bipolar cell axonal territory does not reflect the extension observed at the dendrites.

Next, we counted the number of presynaptic ribbon release sites within individual type 6 bipolar cell axon terminals. To do this, we immunostained for the ribbon synapse-associated protein C-terminal binding protein-2 (CtBP2) (Figure 4A). The number of ribbons in type 6 bipolar cells did not differ between DTR and control retina (Figure 4B; control, 89 ± 22, n = 19 bipolar cells; DTR, 92 ± 26, n = 23 bipolar cells; median ± IQR; p = 0.53, rank sum). This indicates that the number of release sites in type 6 bipolar cells was not affected by the reduced number of cone inputs nor by the reduced mGluR6 expression at the dendrites of these same cells.

To measure the functional impact of partial cone loss on bipolar cell responses, we recorded the *in vivo* electroretinogram (ERG) (Figure S4). While the ERG was unchanged at rod light levels (“Dark-adapted,” left), both the a-wave, driven by photoreceptors, and the b-wave, driven by ON bipolar cells, were significantly reduced at cone light levels (“Light-adapted,” right). This indicates that the population voltage responses of ON cone bipolar cells reflect the loss of cone input. The morphological loss of cone inputs to the type 6 cone bipolar cell dendrites and the stability of its output synapses are consistent with the reduction in the collective ON cone bipolar cell functional output after cone loss. However, the extent to which the perturbations of the type 6 cone bipolar cell dendrites is reflected in the population ERG is unknown.

While synapses with type 6 bipolar cells are stable, $A_{ON\text{-}S}$ ganglion cells could potentially change synapses with other bipolar cell partners (Schwartz et al., 2012; Okawa et al., 2014; Tien et al., 2017). To visualize synapses in these ganglion cells, we biolistically transfected control and DTR retinas with a plasmid encoding fluorescently tagged postsynaptic density (PSD95), a key postsynaptic component of the synapse (Figure 4C). We quantified the density of PSD95 within the dendrites of $A_{ON\text{-}S}$ ganglion cells and found no significant difference between control and DTR retinas (Figure 4D). We also found no change in $A_{ON\text{-}S}$ ganglion cell dendritic arbor complexity as measured by Sholl analysis (data not shown). Despite the loss of synaptic contacts onto the dendrites of type 6 bipolar cells, synapses in the $A_{ON\text{-}S}$ ganglion cells remained morphologically stable. Such morphological stability provides evidence against *de novo* changes arising at the synapses between cone bipolar and ganglion cells after cone loss.

Spatio-Temporal Receptive Fields of $A_{ON\text{-}S}$ Ganglion Cells Widen Spatially and Slow Temporally after Cone Loss

Next, we examined functional properties at the level of the retinal output. We recorded the light responses of dorsal-nasal $A_{ON\text{-}S}$ ganglion cells in whole-cell current clamp. We measured the spatio-temporal receptive fields by presenting a white noise flickering bar stimulus in an intensity range that stimulated cones and recorded membrane voltage (Figures 5A and 5B). Linear-nonlinear modeling was used to calculate temporal filters for the cell’s response at the location of each bar in space, thereby generating a spatio-temporal receptive field map (Figures 5C–5E). The spatial receptive field was extracted by projecting each

point in space onto the first temporal principal component (Figure 5F). Under control conditions, $A_{ON\text{-}S}$ ganglion cells have a narrow depolarizing center and wider hyperpolarizing surround. This basic receptive field structure persists in $A_{ON\text{-}S}$ ganglion cells in DTR retina. To compare the center and surround components, individual spatial receptive fields were fit by a difference of Gaussians (Figure 5F, insets). The receptive fields of ganglion cells in DTR retina had significantly narrower centers (Figure 5H; control, 0.0973 ± 0.046, n = 24 ganglion cells; DTR, 0.0846 ± 0.025 mm, n = 30 ganglion cells; median ± IQR; p = 0.0061, rank sum), wider surrounds (Figure 5I; control, 0.247 ± 0.17; DTR, 0.377 ± 0.043 mm; median ± IQR; p = 0.0044, rank sum), and unchanged center-to-surround weight ratios (Figure 5J; control, 3.41 ± 2.95; DTR, 3.72 ± 2.89; median ± IQR; p = 0.15, rank sum). Additionally, the temporal filters of cells from DTR retina were significantly slower than those of cells from control retina, as measured by an increase in the time to peak of the first temporal principal component (Figures 5G and 5K; control, 0.09 ± 0.02; DTR, 0.10 ± 0.03 s; median ± IQR; p = 0.0049, rank sum). These data provide evidence for functional changes in the receptive fields of ganglion cells after input loss.

While the majority of control cells had receptive fields that were described by principal components that accounted for more than 80% of the variance of the cell's response, this was not true for DTR cells (Figure S5A). Responses with increased variance may result from decreased input due to cone ablation, but they still reflected center-surround organization and could be fit with a difference of Gaussians (Figure S5B). However, 35% of DTR cells had receptive fields without spatial center-surround organization and that could not be fit with a difference of Gaussians (Figure S5C). All of these cells had more than 50% cone loss within their dendritic fields. In contrast, all cells we recorded with less than 50% cone loss in their dendritic fields had receptive fields that could be fit with a difference of Gaussians. These results demonstrate that, up to 50% loss of cones, the general center-surround structure of ganglion cell receptive fields remains intact, while changes do occur in spatial and temporal filtering.

Spatial Receptive Field Adjustments in DTR Retina Are Distinct from Partial Stimulation of Control Retina

Having found changes in the receptive field center and surround widths, we next examined whether such receptive field adjustments could be recapitulated with partial stimulation of the cone mosaic in control retina. If partial stimulation of the cone mosaic in control retina produces similar adjustments in the receptive field as cone loss, then we would conclude that the circuit within DTR retina is like that of control, e.g., these adjustments occur by pre-existing mechanisms of adaptation acting on the receptive field (Enroth-Cugell and Freeman, 1987). In this case, control and DTR retina would be capable of expressing the same receptive field adjustments with either cone loss or partial cone stimulation because the rest of the retinal circuit, aside from the cones, is identical. However, if partial stimulation of the cone mosaic in control retina cannot recapitulate the adjustments observed following cone loss, then we would conclude that the DTR retinal circuit has changed in ways distinct from control retina, i.e., by *de novo* mechanisms not activated by partial stimulation in control retina. To test these two hypotheses, we presented the bar noise stimuli described above and then blanked every other bar to simulate unresponsive cones within the receptive field of

$A_{ON\text{-}S}$ ganglion cells. Blanked bars constantly displayed the intensity of the stimulus mean to hold cones at a uniform level of adaptation.

Comparison between the receptive field profile obtained with full and partial stimulation revealed characteristics distinct from DTR retina (Figures 6A and 6B). Partial stimulation resulted in constant widths for the center (Figure 6C; full, 0.08 ± 0.02; partial, 0.08 ± 0.01 mm; n = 19 ganglion cells; median ± IQR; p = 0.06; sign rank) and surround (Figure 6D; full, 0.24 ± 0.10; partial, 0.20 ± 0.12 mm; median ± IQR; p = 1; sign rank), and no change in the center-to-surround weights of the receptive fields (Figure 6E; full, 5.5 ± 4.38; partial, 4.31 ± 6.29; median ± IQR; p = 1; sign rank). The lack of change in receptive field parameters observed with partial stimulation in control retina is distinct from the narrowing of the center and widening of the surround that was observed in DTR retina (Figures 5H–5J). These results suggest that the DTR retinal circuit exhibits *de novo* changes distinct from the control retinal circuit. Partial stimulation also resulted in a slower temporal filter as compared to full stimulation (Figure 6F; full, 0.09 ± 0.01; partial, 0.1 ± 0.01 s; median ± IQR; n = 19; p = 0.011; sign rank). This change is congruent with the slower temporal filter observed in DTR versus control retina (Figure 5K). This suggests that the temporal changes to ganglion cell receptive fields are the product of a mechanism pre-existing within the mature retinal circuit. Taken together, these results indicate that the mature retinal circuit exhibits both *de novo* changes after input loss that affect spatial processing and pre-existing mechanisms that affect temporal processing.

To understand where in the retinal circuit these *de novo* changes in receptive field arise, we recorded the excitatory and inhibitory input currents onto $A_{ON\text{-}S}$ ganglion cells from control and DTR retina in response to the full receptive field stimulus (Figure 7). We found that the two characteristic changes we observed in the voltage receptive fields each derived from a different source: the decrease in center width was present in only the excitatory current receptive fields (Figure 7E), and the increase in surround width was present only in the inhibitory current receptive fields (Figures 7F and 7J). This indicates that the narrower center is inherited through excitation onto the ganglion cell, i.e., bipolar cell input, while the wider surround is inherited through direct inhibition onto the ganglion cell, i.e., through amacrine cell input. We also found that the center-to-surround weight ratio for excitation is significantly higher in DTR retina than in control retina, unlike in either the voltage or the inhibitory receptive fields (Figures 7G and 7K). This change in ratio is driven by weaker surround weights, suggesting that horizontal cell contribution to the surround is weaker after cone loss. However, the voltage receptive fields do not exhibit this change in ratio, suggesting that the center-to-surround balance is restored by the retinal output. Both excitation and inhibition displayed the slower time to peak seen in voltages from DTR retina and partially stimulated control retina (Figures 7H and 7L). These results identify the excitatory and inhibitory pathways converging onto the ganglion cell as both contributing to the receptive field changes following partial cone loss.

DISCUSSION

Understanding the mature retinal circuit's response to loss of cones requires temporal control over cone death. In our previous work with laser ablation of cones, we found that

mGluR6 disappears selectively from the dendritic terminals where cones have been lost within the first 24 h (Dunn, 2015). In the present work, with the DTR model, we extend our window of observation by ablating cones *in vivo* and waiting 3 to 60 days before examining the retina (Figure 1). In this longer time window, we observe that, within 3 days of cone ablation, type 6 cone bipolar cell dendrites remodel. Some type 6 bipolar dendrites that lose cone contact simplify, while others extend and possibly form new synapses (Figure 2). We also observe that the mGluR6 distribution is still dendrite-specific and cone-dependent (Figure 3). These changes are consistent with a mechanism that independently regulates each dendrite and depends on the presence or absence of a cone contact on that dendrite. Despite this rearrangement of the first-order synapse in the cone pathway, we observed structural stability in the morphology and the number of presynaptic release sites in the type 6 bipolar cell axons (Figure 4). This suggests that changes in the number and spatial arrangement of inputs to type 6 bipolar cells are not reflected in the number and spatial arrangement of their outputs. Furthermore, we found postsynaptic densities were maintained within the $A_{ON\text{-}S}$ ganglion cells that receive the majority of their input from type 6 cone bipolar cells (Figure 4). Despite this stability of the second-order synapse of the cone pathway, we found $A_{ON\text{-}S}$ ganglion cells exhibited adjustments in their cone-mediated voltage responses (Figure 5). $A_{ON\text{-}S}$ ganglion cells had significant changes to their spatial receptive fields. These spatial changes in DTR retina were distinct from those observed in control retina with partial stimulation (Figure 6), suggesting that the mechanism(s) are *de novo* rather than pre-existing within the retinal circuit. Indeed, when we examined the input currents to $A_{ON\text{-}S}$ ganglion cells, we found that a dominant underlying mechanism for the expansion of the receptive field surround involves inhibitory circuits (Figure 7).

Developmental Versus Mature Reactions to Input Loss

Here, we report that the loss of cones is capable of triggering postsynaptic dendritic remodeling, including growth, in type 6 bipolar cells. The mechanism that induces growth in these dendrites remains unknown. Neurotransmission has been demonstrated throughout the nervous system to be capable of inducing calcium-mediated cytoskeletal changes and subsequent dendritic remodeling (Sorensen and Rubel, 2006; reviewed in Wong and Ghosh, 2002). Membrane-bound factors such as cell adhesion and chemotactic molecules are also able to modulate dendritic morphology (Sweeney et al., 2011).

In a recent study using photocoagulation in mature rabbit retina, Beier et al. (2017) reported a capacity for rod bipolar cells to form synapses with photoreceptors outside the lesion; however, the cone bipolar cells they examined did not exhibit the same remodeling capacity. With our different method of ablation and visualization of cone bipolar cells, we did observe remodeling. If we had observed only retraction of dendrites, that would have been evidence for gradual degradation of bipolar cells and their circuits. Instead, we see retraction of some dendrites alongside the persistence and growth of other dendrites, indicating that bipolar cell dendrites may be seeking viable synaptic partners. Indeed, we found abnormally long dendrites in DTR retina contacting cones with mGluR6 localized to the contact site, suggesting that dendrites may have formed new synapses with more distant cones, although we cannot rule out the possibility that these synapses were pre-existing and have simply translocated away from the bipolar cell; however, translocation of photoreceptors has not

been observed (Han et al., 2012; Sher et al., 2013). A previous study eliminating cone transduction demonstrated that cone bipolar cells will make ectopic synapses with existing rods (Haverkamp et al., 2006). However, the study did not distinguish whether these synapses were formed during development or in the fully mature retina. Because we ablated cones in mature retina, we conclude that dendritic growth can be induced in bipolar cells after initial synapse development, as type 6 ON cone bipolar cells find their appropriate synaptic partners by P13 in the mouse (Dunn and Wong, 2012). This supports the assertion that the mature retina has some capacity for remodeling to replace lost synaptic partners.

Another contrasting result is the coordination of input and output synapses observed with developmental perturbations. It has been shown that the number of presynaptic release sites in type 6 bipolar cell axon terminals can increase or decrease based on the level of spontaneous activity incident on bipolar cells in germline mutations (Kerschensteiner et al., 2009; Soto et al., 2012). Despite decreased numbers of input to type 6 bipolar cells in our manipulation, we do not see an increase or decrease in the number of presynaptic release sites. This indicates either that the decrease in inputs does not alter spontaneous activity enough to activate this mechanism, or that this mechanism is not present in mature type 6 bipolar cells.

Relationship to Retinal Disease

Mice have been widely used to understand human outer retinal diseases. The challenge remains in the interpretation of effects on the retina across organisms with vast differences in life span and onset of retinal degeneration. Cone loss has been identified as the instigator for broader retinal damage (Marc and Jones, 2003). Here, our methods allowed us to test whether partial cone loss would cause rearrangement of the retina. We limited our observation to 2 months after DT injection. In this period, we did not see obvious rearrangement of the inner retina, as evidenced by intact axons stratifying in the appropriate layers and gross anatomy of retinal layers (Figure S1). However, the acute and limited cell loss induced by DT injection may not mimic the slow and severe death observed in certain types of retinal degeneration. Nevertheless, our data suggest several salient findings that may inform the development and optimization of therapies for retinal degeneration: (1) type 6 cone bipolar cells preferentially contact cones following cone death, increasing the likelihood of successful synaptic integration of newly transplanted photoreceptors in cellular therapies; (2) structural and synaptic features of the bipolar cell to retinal ganglion cell synapse are intact even after an extended period of cone loss, enabling therapeutic strategies that either aim to replace lost cones or interface directly, through optogenetics or prosthetic devices, with bipolar cells to restore phototransduction to the retinal circuit; (3) $A_{ON\text{-}S}$ ganglion cells maintain center-surround receptive field structure at least through 50% cone loss, opening the possibility of developing strategies that specifically target these cells; (4) overall, the degree of retinal remodeling is relatively limited in comparison to previous reports made over longer time windows, suggesting that vision restoration therapies may have increased efficacy earlier in the disease course. Furthermore, at these early stages, the functional resilience observed in our study may help explain why patients with photoreceptor degeneration do not report visual deficits until the majority of photoreceptors

are gone, and suggest that resilience within the visual system may arise first within the retina.

Potential Compensatory Circuit Changes

In DTR retina, we observed what might be considered a compensatory gain of function in the cone-mediated ganglion cell receptive field. By removing 50%–75% of cones, our manipulation effectively decreases the cone-mediated signal-to-noise ratio at ganglion cells. The efficient coding hypothesis laid out by Atick and Redlich (1990) predicts that the optimal receptive field for ganglion cells has a wider, weaker surround as the signal-to-noise ratio decreases. The increased size of the surround that we observe in the receptive fields of ganglion cells from DTR retina is consistent with these predictions.

Atick and Redlich's efficient coding hypothesis further predicts that the optimal receptive field for ganglion cells at an even lower signal-to-noise ratio should be a single wide Gaussian without a spatially opponent surround. Indeed, we observed that one-third of ganglion cells in DTR retina could not be captured by a difference of Gaussians and exhibited a wide receptive field best captured by a single Gaussian (Figure S5C). These ganglion cells in the no-fit category often had far fewer remaining cones within the dendritic field than those in the categories where a difference of Gaussians could be fit. Thus, those ganglion cells in the no-fit category could be considered the condition with the lowest signal-to-noise ratio. The widening of the surround and the eventual loss of a spatially opponent receptive field we observe are consistent with theory and indicate that the receptive field changes we see may maintain better signal encoding in the cone-depleted retina.

Atick and Redlich's efficient coding hypothesis also predicts an increase in the size of the center, which our data did not show. An increase in center size consistent with theory may require formation of new excitatory synapses, evidence of which we did not see at these time points at the first- nor second-order synapses within retina. The adjustments in receptive field sizes in DTR retina could be explained by a loss in excitatory synapses, originating at the cone-to-cone bipolar cell synapses, which contribute to the center, and a gain in inhibitory synapses, which contribute to the surround. In our examination of excitatory and inhibitory input currents that contribute to the voltage receptive field, we identified the potential sources of receptive field changes following partial cone loss in mature retina. First, the narrower receptive field center of excitatory inputs, via bipolar cell input, suggests that the rare observation of bipolar cell dendritic extension is not reflected in the receptive field profiles across the population of ganglion cells (Figures 2H and 7E). Second, the decrease in center-to-surround ratio and the constant surround width in the receptive field of excitatory inputs suggests that the spatial contribution of horizontal cells to the surround has not changed while the weight of its influence has diminished following cone loss (Figures 7F and 7G). Consistent with this interpretation, horizontal cell populations were morphologically unaffected in DTR retina (Figure S2A; Table S1). This decrease in surround weight could potentially compensate for the loss of bipolar cell input observed in the ERGs. Finally, the wider receptive field surround of inhibitory inputs, via amacrine cells, suggests that direct amacrine cell influence on ganglion cells has expanded following partial cone loss (Figure 7J). Such an expansion could arise from *de novo* inhibitory synapses with

pre-existing or new amacrine cell partners with the $A_{ON\text{-}S}$ ganglion cells. Such changes in the receptive field structure are consistent with the greater dynamics of inhibitory circuits compared to excitatory circuits in visual cortex following monocular deprivation (Villa et al., 2016). Villa et al. proposed that the modulation of activity following changes in sensory input may be more parsimoniously achieved by adjusting lateral inhibitory synapses compared to feedforward excitatory synapses, and our findings are consistent with their proposal. These results will direct our future studies of the compensatory mechanisms active in the retina after cone loss to the amacrine cell inputs onto these ganglion cells.

Stability and Plasticity across CNS Circuits

As Wandell and Smirnakis (2009) aptly wrote, “There can be no serious debate as to whether the brain is plastic or not: it is both. It is more worthwhile to investigate distinct systems and understand conditions under which each system is plastic or stable.” Previous work on sensory deprivation has reported cortical rewiring of both excitatory and inhibitory circuits (Keck et al., 2008, 2011, 2013; Hickmott and Merzenich, 2002; reviewed in Harding-Forrester and Feldman, 2018). Lack of evidence for rewiring in the mature retina and lateral geniculate nucleus in vision (Eysel, 1982) and in thalamus in somatosensation (Wallace and Fox, 1999; Wallace et al., 2001) reduced the interest in searching for pre-cortical mechanisms of plasticity. Here, we have revived the search for plasticity within retina, and indeed we find supporting evidence with dendritic remodeling in bipolar cells and with *de novo* changes to the ganglion cell receptive field structure following input loss. While we also find evidence in support of pre-existing mechanisms to withstand partial cone loss, e.g., stability of synaptic structures at the second-order synapse, our results highlight that circuits of the retina and lateral geniculate nucleus may not be distinct from those in cortex with respect to the capacity for plasticity. Rather, these circuits are subject to similar constraints. A comprehensive body of work demonstrating cortical rewiring following sensory deprivation showed that remodeling is possible only after partial retinal lesions, rather than complete retinal ablation (Keck et al., 2008, 2011,2013; but see Horton and Hocking, 1998; Smirnakis et al., 2005). In other words, persistence of existing activity is necessary to induce and regulate plasticity, as has been demonstrated in developing visual cortex (Reiter et al., 1986; Hata et al., 1999) and the adult somatosensory cortex (Wallace and Fox, 1999). Complete loss of sensory input also failed to induce remodeling in mature visual cortex (Keck et al., 2008, 2011, 2013). Our system of ablation spared a random population of cones, which could be distinct from previous methods of focal laser lesion (Beier et al., 2017). Indeed, our targeted cone ablation may have been appropriately sparse to induce plasticity/compensation and/or uncover preexisting mechanisms, e.g., redundancy or adaptation, that underlie resilience in specific retinal circuits.

With the unique accessibility to a specific circuit, we have demonstrated both plasticity and stability, likening the retina to the rest of the brain in this respect. The cell-type-specific accessibility of the retina allowed us to garner insights about the contributions of individual synapses to functional resilience of a circuit following input loss.

STAR★METHODS

CONTACT FOR REAGENT AND RESOURCE SHARING

Further information and requests for resources and reagents should be directed to and will be fulfilled by the Lead Contact, Felice Dunn (Felice.Dunn@ucsf.edu).

EXPERIMENTAL MODEL AND SUBJECT DETAILS

Mice—All procedures were done in accordance with the University of California, San Francisco and the University of Washington Institutional Animal Care and Use protocols. The following transgenic mouse lines were crossed: *OPN1SW-Cre* (Akimoto et al., 2004) for Cre-recombinase expression in cones containing S opsin or *OPN1MW-Cre* (Le et al., 2004) for Cre-recombinase expression in cones containing M opsin, *Rosa26-loxP-stop-loxP-DTR* (Buch et al., 2005) for Cre-dependent expression of the diphtheria toxin receptor, *hLMcone-GFP* for visualization of cones containing M opsin (Fei and Hughes, 2001) or *Ai6* as a reporter for the Cre expression (Madisen et al., 2010), and *Grm6-TdTomato* for visualization of a sparse population of ON bipolar cells (Kerschensteiner et al., 2009). The *Grm6-TdTomato* line labels a variable number of type 5, 6, 7, 8 ON cone bipolar cells and rod bipolar cells. When crossed to a fluorescent reporter line *Ai6*, the *OPN1SW-Cre* revealed labeled cone photoreceptors and a small population of rod photoreceptors, amacrine cells, and ganglion cells (Figures S1G–S1K). When crossed to a fluorescent reporter line *Ai6,* the *OPN1MW-Cre* revealed labeled cone photoreceptors and a dozen neurons in the ganglion cell layer across the entire retina (Figures S1L–S1P). All transgenic mice were backcrossed into the *C57BL/6J* background. Mice lacking either the Cre-recombinase or DTR or both, with either diphtheria toxin or saline injection, were used as littermate controls. Mice that had all 4 genotypes *OPN1SW-Cre or OPN1MW-Cre* × *Rosa26-loxP-stop-loxP-DTR* × *hLMcone-GFP or Ai6* × *Grm6-TdTomato* were used for cone ablations. Male and female mice were used for experiments. Between P30-35 mice were anesthetized with 1%–4% isoflurane, weighed, and injected with diphtheria toxin at dosages of 100ng/g. Injections were made intramuscularly into the quadriceps. Double injections were given 1-4 days apart into the quadriceps of different legs. The animals were monitored daily following diphtheria toxin injection. Mice survived for intervals between 3 days and 2 months following the second toxin injection.

METHOD DETAILS

Tissue preparation for immunostaining—Mice were euthanized by isoflurane overdose or carbon dioxide followed by cervical dislocation. The mice were enucleated and the retinas were dissected and mounted on nitrocellulose filter paper (Millipore) in bicarbonate-based Ames solution equilibrated with 95% O_2/5% CO_2. The orientation and sidedness of retinas were noted so that dorsal-ventral and temporal-nasal axes could be distinguished in the whole mount retina. The retinas were fixed in 4% paraformaldehyde for 15 min or 2% paraformaldehyde for 20 min at room temperature, rinsed in PBS, pH 7.42, then immersed in blocking solution (5% normal donkey serum, 0.5% Triton X-100 in PBS) overnight, incubated in primary antibodies for 5 days at 4°C, then rinsed in PBS and incubated in secondary antibodies for 1 day at 4°C, and rinsed with PBS and mounted with Vectashield underneath a coverslip. For quantification of cell types in sections, the whole

eye was fixed in 4% paraformaldehyde for 90 min, 20 μm frozen sections were rinsed in PBS, incubated in primary antibodies for day at 4°C, rinsed with PBS, incubated in secondary antibody for 1 hr at room temperature, rinsed with PBS, and mounted with Vectashield underneath a coverslip. Reagents are listed in the Key Resources Table.

Biolistic transfection—Mice were anesthetized by carbon dioxide overdose, euthanized by cervical dislocation, and enucleated. Retinas were dissected in oxygenated mouse ACSF and mounted whole on filter paper. DNA coated gold particles were prepared by coating 12.5 mg of 1.6 mm gold particles (Bio-Rad) with 20 μg of *CMV:CFP* and 7 μg of *CMV:PSD95-YFP* plasmids. A suspension of DNA-coated gold particles in ethanol was precipitated onto the inner surface of Teflon tubing (Bio-Rad) and subsequently cut into 12-mm segments. A Helios gene gun (Bio-Rad) was used to biolistically deliver plasmid-coated gold particles to whole-mounted retinas. Gold particles were propelled onto the tissue using helium gas at 40 psi. Retinas were then transferred to an oxygenated and humidified chamber and maintained for 27 h at 30°C to allow fluorescent protein to be sufficiently expressed for subsequent imaging (Santina and Ou, 2018). Once sufficient expression was observed, retina were fixed in 4% paraformaldehyde for 15 min and immunostained according to the procedure described above.

Confocal imaging—To image type 6 bipolar cells, genetically-encoded fluorescence in the retinas was first viewed through the eyepieces using epifluorescence. Isolated type 6 bipolar cells were identified by their distinct axonal morphology (Dunn and Wong, 2012). Bipolar cells were chosen by high signal-to-noise ratio of the bipolar fluorescence without regard to the cone density in the immediate vicinity. Isolated bipolar cells in the retina were imaged on a Zeiss LSM700 confocal microscope or a Leica SP8 with the oil immersion 63x (NA 1.4) objective. High-resolution image stacks were taken of the bipolar cell dendrites with voxel sizes of 0.05-0.08 μm/pixel (x axis, y axis) and 0.2 μm/pixel (z axis). Lower resolution image stacks were taken of the entire bipolar cell to verify cell type 0.10 μm/pixel (x axis, y axis) and 0.4 mm/pixel (z axis). Each plane was acquired 2-4 times to obtain the average.

To image the biolistically-transfected ganglion cells, we identified cells with bright fluorescent expression first through the eyepieces using epifluorescence and mapped their location in the retina. To identify $A_{ON\text{-}S}$ ganglion cells, we chose ganglion cells with large polygonal somas colocalized with SMI-32 and whose dendrites stratified within the type 6 ON cone bipolar cell axon layer of synaptotagmin-2 (Syt2) staining. We used the 40x (NA 1.3) objective on a Leica SP8 to acquire image stacks at 0.098 × 0.098 × 0.3 μm/pixel.

Electrophysiology tissue preparation—Mice were dark-adapted overnight. Dissections were performed in the dark with infrared illumination and image converters. Mice were euthanized by cervical dislocation and enucleated. Retinas were dissected in warmed bicarbonate-based Ames solution, equilibrated with 95% O_2/5% CO_2, and cut into halves or quadrants to keep track of sidedness and topography. To control for topographical variation in ganglion cell size, recordings were made in dorsal-nasal retina where the largest alpha ON-sustained ganglion cells (abbr. $A_{NO\text{-}S}$) ganglion cells reside (Bleckert et al., 2014). For patch-clamp recordings, retina quadrants were stored in a light-tight chamber with the

retinal pigment epithelium attached in equilibrated bicarbonate-based Ames heated to 32°C for 30 minutes before recording. The retinal pigment epithelium was then removed, retina quadrants were mounted ganglion cell side up on glass coverslips and continuously perfused at 8-10 mL/min with equilibrated bicarbonate-based Ames heated to 35°C. After recordings, retina were mounted on filter paper and processed for immunostaining and imaging as described above.

Patch-clamp recordings—Patch electrodes were pulled from borosilicate glass (Sutter Instruments) on a DMZeitz or Narishige puller to 3 MOhm resistance. Cells in the ganglion cell layer were targeted based on their large polygonal somas visualized under infrared light (950nm). An empty patch pipette was used to dissect away the inner limiting membrane to expose cells for recording. Targeted cells were first recorded in cell-attached configuration with an electrode filled with HEPES buffered Ames. This configuration allowed for recording of extracellular spikes from the targeted cells. Following cell-attached recordings, the same targeted cells were recorded in current clamp with a patch pipette filled with internal solution containing (in mM): 104.7 cesium methane sulfonate, 10 TEA Cl, 20 HEPES, 10 EGTA 2, QX-314, 5 ATP, 0.5 GTP, adjusted to pH 7.3 with CsOH and the 0.04% Lucifer Yellow dye. Signals were amplified with an Axopatch MultiClamp 700B amplifier (Molecular Devices, Palo Alto, CA), digitized with an Instrutech ITC-18, and acquired with Symphony.

Cell identification—$A_{ON\text{-}S}$ ganglion cells were identified during recording by their characteristic sustained spiking response to a 500ms light step. Putative $A_{ON\text{-}S}$ ganglion cells were confirmed after recording with immunolabeling for SMI-32, a neurofilament marker that labels alpha-type cells and for Syt2, a calcium sensor found in the axon terminals of type 6 ON cone bipolar cells, which co-stratify with the dendrites of $A_{ON\text{-}S}$ ganglion cells.

Light stimuli—Light stimuli were generated by a DLP Lightcrafter projector (Texas Instruments DLPLCR4500EVM). The projector stimulus had red, green, and blue LED (420-700nm) output more effective for driving M opsin than S opsin (Wang et al., 2011). Spatial stimuli were created in Stage and consisted of binary flickering bars (width of 40μm) whose intensity was drawn from a Gaussian distribution with mean intensity of 8,400 Rh*/rod/sec and standard deviation 0.3. Stimuli were generated from random seeds and were shown for 50 s.

Electroretinogram recordings—Mice were dark adapted overnight. On the day of experiment, mice were anesthetized with i.p. injection of Ketamine/Xylazine (80mg/kg, 10mg/kg, respectively) and positioned on the recording apparatus (Celeris, Diagnosys LLC, Gaithersburg, MD). Pupils were dilated using drops of 1% tropicamide and corneas protected by application of a thin layer of methylcellulose. Body temperature was constantly maintained at 37°C with a heating pad.

Electroretinograms (ERGs) were recorded in complete darkness via coiled silver electrodes making contact with the moist cornea. A gold needle electrode was placed under the skin between shoulders to serve as both reference and ground. Responses were amplified

differentially, band-pass filtered (0.1 to 500 Hz), digitized at 10 kHz and stored on disk for processing. Responses to flashes were averaged with an interstimulus interval ranging from 2 s for dim lights to 10 s for the brightest flashes. Five responses were averaged for each light intensity to eliminate electrical noise.

Full field illumination of the eyes was achieved with the miniaturized Ganzfeld spheres integrated with the recording electrodes (Celeris Bright RGB stimulators, Diagnosys LLC). Brief (10ms) white flashes were delivered under dark adapted and light adapted conditions, generating the typical flash ERG response ranging from 0.33 to 97 photons*μm^{-2}*s^{-1} (Makous, 1997). ERG waveforms were stored to disk and analyzed by measuring a- and b-wave amplitudes and their relative implicit times. The a-wave was measured from baseline to the trough of the first negative peak and the b-wave was measured from the a-wave peak to the peak of the large positive wave.

QUANTIFICATION AND STATISTICAL ANALYSIS

Image analysis of bipolar cells—Image stacks were median filtered (3 pixels). The bipolar cell, cone, and mGluR6 channels were interpreted into three-dimensional binary masks using Amira (FEI) (Dunn et al., 2013). Each cone within the bipolar cell's dendritic field was labeled with a unique identity. The binary masks were analyzed with custom-written routines in MATLAB (Mathworks) for the volume overlap between bipolar dendrites and cones. Nonzero overlap between the bipolar cell and cone channel determined whether a contact was made. The binary mask was used to perform the following analyses manually: primary branch length, claw count, number of secondary branches, area of the dendritic and axonal territories. Primary branch lengths were analyzed in FIJI using Simple Neurite Tracer to trace the dendrite in three dimensions along the longest route from the soma to the dendritic tip. Claws were defined as any 3 branches within a 10 μm diameter circle. Higher order branches (second-order and greater branches) were counted that fell outside a claw.

Quantification of cone numbers—To count cones in ganglion cell dendritic fields, image stacks were loaded into Imaris (Bitplane) and the Spots function was used. The count was checked and corrected manually.

Quantification of synaptic density—To measure the synaptic puncta within the bipolar cell axon, images of individual type 6 bipolar cell axons were binarized (Amira). Presynaptic CtBP2 puncta within the axonal region were manually counted in a maximum projection with FIJI's Cell Counter plug-in.

To measure ganglion cell dendritic arbor parameters and count postsynaptic puncta, images of individual $A_{ON\text{-}S}$ ganglion cells were skeletonized in Imaris and dendritic parameters were measured from a two-dimensional projection of the skeleton using custom MATLAB routines (Della Santina et al., 2013). Dendritic area was defined as the area of the convex hull enclosing the dendritic arbor. Dendritic complexity was calculated using the Sholl analysis function within Imaris. To determine PSD95-YFP puncta distribution on dendrites of individual ganglion cells, we used a semiautomated method for quantifying synapse density as previously described (Morgan et al., 2008), with modifications (Object Finder; Della Santina et al., 2013). ImageJ was used to median filter the images to remove the

thermal noise from the microscope's photomultipliers. Using the 3D dendritic skeleton generated in Imaris, custom-written MATLAB routines then created a binary mask to include PSD95-YFP signal only within the dendrites of the ganglion cell of interest. Details of candidate puncta identification and final validation are previously described (Della Santina et al., 2013). Linear density of puncta as a function of distance from the cell soma is calculated by quantifying puncta density along the dendritic skeleton within a moving window of 10 μm.

Quantification of cell death—To count photoreceptor and interneuron cell bodies, mice were euthanized and eyes enucleated and immediately immersed in cold fixative (2% PFA, 2.5% glutaraldehyde, and 0.1 M phosphate buffer, pH 7.4) for 24 hours, after which they were transferred to cold 0.1 M phosphate buffer and dehydrated in graded ethanol. Samples were embedded in Technovit 7100 Glycol Methacrylate (Electron Microscopy Sciences, Hatfield, PA) and serial sagittal sections (3 μm) passing through the optic nerve were cut and stained with Hematoxylin and Eosin (H&E). For each retina, the number of cell bodies in the inner nuclear layer and outer nuclear layer was obtained by averaging four measurements taken from two cross sections from the same eye. Measurements from both nuclear layers were taken at equidistant points around the eye approximately 3/8 of the distance between the optic nerve and the periphery, i.e., slightly short of the midpoint. These values were used for statistical analysis for control and DTR conditions (Figures S1Q–S1T).

To visualize retinal cell populations in the flat mount and sectioned retina, we immunostained for bipolar (PKC alpha; Syt2), horizontal (calbindin), amacrine (syntaxin-1) and ganglion cells (RBPMS), and Müller glia (Sox9; GFAP) and microglia (Iba1; CD68). Quantification was either done in Fiji with Cell Counter or in Imaris with the Spots function. These values were used for statistical analysis for control and DTR conditions (Table S1).

Electrophysiology analysis: spatio-temporal receptive field maps—To measure the receptive field we followed Baccus and Meister (2002). Briefly, the linear temporal filters were computed for the location in space of each of the bars of the stimulus by correlating the stimulus at that location over time with the response, and dividing by the autocorrelation of the stimulus to normalize for a finite stimulus presentation. The nonlinearity was found by plotting the actual response amplitude by the predicted response amplitude, and smoothing across neighboring points after sorting by the predicted response amplitude. The spatio-temporal receptive field maps were generated by arranging the temporal filters according to the corresponding spatial location of the stimulus.

To extract the spatial receptive field we used principal components analysis. All temporal filters were projected along the first principal component of the temporal filters (capturing at least 60% of the variance of the filters) to generate the cell's spatial receptive field. To increase the signal, particularly of the surround, we assumed that the spatial receptive field was symmetric and averaged the two sides of the receptive field about the midline. The resulting shape was fit with a difference of Gaussians. The parameters of this fit describe the size and weight of the center Gaussian and surround Gaussian and statistical tests were performed across control and DTR conditions (rank sum). Parameters were used to generate

the receptive field Gaussians for each ganglion cell, where w_c (w_s) is the center (surround) weights, and $_c$ (σ_s) is the center (surround) standard deviation width.

$$y = w_c \exp\left(\frac{-X^2}{2\sigma_c^2}\right) - w_s \exp\left(\frac{-X^2}{2\sigma_s^2}\right)$$

For partial stimulation experiments (Figure 6), every other bar was held constant at the mean intensity value while neighboring bars varied in intensity. Subsequent analysis was identical to that described above. Receptive field parameters were compared for the same cells stimulated with the full bar array or partially blanked bar array.

Statistical analysis—Data presented as median ± interquartile range (IQR). Histograms are plotted with bin values to the left of each bar (Figures 1,2, 3, and 4). Medians are indicated by arrowheads on top of the histograms. A Wilcoxon rank sum test (abbr. rank sum) was used to identify significant differences between conditions. A Wilcoxon sign rank test (abbr. sign rank) was used to identify significant differences between conditions with paired data (Figure 6). All p values are indicated in the Results. Asterisks in Figures indicate the following p values: * ≤ 0.05, ** ≤ 0.01, *** ≤ 0.005.

DATA AND SOFTWARE AVAILABILITY

Software used to analyze the PSD95 puncta on ganglion cells can be found at https://lucadellasantina.github.io/ObjectFinder/. Software used to acquire physiology data can be found at https://github.com/Symphony-DAS/symphony-v1/wiki. Software used to drive the projector can be found at https://github.com/Stage-VSS/stage-v1.

Supplementary Material

Refer to Web version on PubMed Central for supplementary material.

ACKNOWLEDGMENTS

We thank Rachel O. L. Wong and Haruhisa Okawa for enabling this project; Jonah Chan, David Copenhagen, Jonathan Horton, Joo Yeun Lee, Fred Rieke, Joshua Sanes, Michael Stryker, and Weiwei Wang for critical reading of the manuscript; Mark Cafaro, Mei Zhang, John Campbell, Grace Yang, and Jessica Wong for technical assistance; Ivan Anastassov, Jeanette Hyer, and Jacque Duncan for helpful discussions; Catherine Morgans, Melina Agosto, Theodore Wensel, and Kirill Martemyanov for sharing reagents; and Joo Yeun Lee and Suling Wang for help with the graphical abstract. This work was supported by NIH through grants T32EY007120 and F31EY028017 (R.A.C.); R25MH060482 (D.B.K.); EY-017101, P30 EY-01730, T32HD007183, and EY-07031 (C.G.); Vision Core Grant P30 EY-002162 (UCSF); and EY-029772 (F.A.D.); and by foundation grant support from Klingenstein-Simons Fellowship, E. Matilda Ziegler Foundation, McKnight Foundation, Research to Prevent Blindness Career Development Award and Unrestricted Grant, and That Man May See.

REFERENCES

Akimoto M, Filippova E, Gage PJ, Zhu X, Craft CM, and Swaroop A (2004). Transgenic mice expressing Cre-recombinase specifically in M- or S-cone photoreceptors. Invest. Ophthalmol. Vis. Sci 45, 42–47. [PubMed: 14691152]

Applebury ML, Antoch MP, Baxter LC, Chun LL, Falk JD, Farhangfar F, Kage K, Krzystolik MG, Lyass LA, and Robbins JT (2000). The murine cone photoreceptor: a single cone type expresses both S and M opsins with retinal spatial patterning. Neuron 27, 513–523. [PubMed: 11055434]

Atick JJ, and Redlich AN (1990). Towards a theory of early visual processing. Neural Comput. 2, 308–320.

Baccus SA, and Meister M (2002). Fast and slow contrast adaptation in retinal circuitry. Neuron 36, 909–919. [PubMed: 12467594]

Beier C, Hovhannisyan A, Weiser S, Kung J, Lee S, Lee DY, Huie P, Dalal R, Palanker D, and Sher A (2017). Deafferented adult rod bipolar cells create new synapses with photoreceptors to restore vision. J. Neurosci 37, 4635–4644. [PubMed: 28373392]

Bleckert A, Schwartz GW, Turner MH, Rieke F, and Wong ROL (2014). Visual space is represented by nonmatching topographies of distinct mouse retinal ganglion cell types. Curr. Biol 24, 310–315. [PubMed: 24440397]

Buch T, Heppner FL, Tertilt C, Heinen TJAJ, Kremer M, Wunderlich FT, Jung S, and Waisman A (2005).A Cre-inducible diphtheria toxin receptor mediates cell lineage ablation after toxin administration. Nat. Methods 2, 419–426. [PubMed: 15908920]

Della Santina L, Inman DM, Lupien CB, Horner PJ, and Wong RO (2013). Differential progression of structural and functional alterations in distinct retinal ganglion cell types in a mouse model of glaucoma. J. Neurosci 33, 17444–17457. [PubMed: 24174678]

Dunn FA (2015). Photoreceptor ablation initiates the immediate loss of glutamate receptors in postsynaptic bipolar cells in retina. J. Neurosci 35, 2423–2431. [PubMed: 25673837]

Dunn FA, and Wong ROL (2012). Diverse strategies engaged in establishing stereotypic wiring patterns among neurons sharing a common input at the visual system's first synapse. J. Neurosci 32, 10306–10317. [PubMed: 22836264]

Dunn FA, Della Santina L, Parker ED, and Wong RO (2013). Sensory experience shapes the development of the visual system's first synapse. Neuron 80, 1159–1166. [PubMed: 24314727]

Enroth-Cugell C, and Freeman AW (1987). The receptive-field spatial structure of cat retinal Y cells. J. Physiol 354, 49–79.

Eysel UT (1982). Functional reconnections without new axonal growth in a partially denervated visual relay nucleus. Nature 299, 442–444. [PubMed: 7121581]

Fei Y, and Hughes TE (2001). Transgenic expression of the jellyfish green fluorescent protein in the cone photoreceptors of the mouse. Vis. Neurosci 15, 615–623.

Han DP, Croskrey JA, Dubis AM, Schroeder B, Rha J, and Carroll J (2012). Adaptive optics and spectral-domain optical coherence tomography of human photoreceptor structure after short-duration [corrected] pascal macular grid and panretinal laser photocoagulation. Arch. Ophthalmol 130, 518–521. [PubMed: 22491923]

Harding-Forrester S, and Feldman DE (2018). Somatosensory maps. Handb. Clin. Neurol 151, 73–102. [PubMed: 29519481]

Hata Y, Tsumoto T, and Stryker MP (1999). Selective pruning of more active afferents when cat visual cortex is pharmacologically inhibited. Neuron 22, 375–381. [PubMed: 10069342]

Haverkamp S, Michalakis S, Claes E, Seeliger MW, Humphries P, Biel M, and Feigenspan A (2006). Synaptic plasticity in CNGA3$^{-/-}$ mice: cone bipolar cells react on the missing cone input and form ectopic synapses with rods. J. Neurosci 26, 5248–5255. [PubMed: 16687517]

Hickmott PW, and Merzenich MM (2002). Local circuit properties underlying cortical reorganization. J. Neurophysiol 55, 1288–1301.

Horton JC, and Hocking DR (1998). Monocular core zones and binocular border strips in primate striate cortex revealed by the contrasting effects of enucleation, eyelid suture, and retinal laser lesions on cytochrome oxidase activity. J. Neurosci 18, 5433–5455. [PubMed: 9651225]

Jeon CJ, Strettoi E, and Masland RH (1998). The major cell populations of the mouse retina. J. Neurosci 15, 8936–8946.

Johnson RE, Tien N-W, Shen N, Pearson JT, Soto F, and Kerschensteiner D (2017). Homeostatic plasticity shapes the visual system's first synapse. Nat. Commun 8, 1220. [PubMed: 29089553]

Keck T, Mrsic-Flogel TD, Vaz Afonso M, Eysel UT, Bonhoeffer T, and Hubener M (2008). Massive restructuring of neuronal circuits during functional reorganization of adult visual cortex. Nat. Neurosci 11, 1162–1167. [PubMed: 18758460]

Keck T, Scheuss V, Jacobsen RI, Wierenga CJ, Eysel UT, Bonhoeffer T, and Hübener M (2011). Loss of sensory input causes rapid structural changes of inhibitory neurons in adult mouse visual cortex. Neuron 71, 869–882. [PubMed: 21903080]

Keck T, Keller GB, Jacobsen RI, Eysel UT, Bonhoeffer T, and Hübener M (2013). Synaptic scaling and homeostatic plasticity in the mouse visual cortex in vivo. Neuron 80, 327–334. [PubMed: 24139037]

Kerschensteiner D, Morgan JL, Parker ED, Lewis RM, and Wong ROL (2009). Neurotransmission selectively regulates synapse formation in parallel circuits in vivo. Nature 460, 1016–1020. [PubMed: 19693082]

Le Y-Z, Ash JD, Al-Ubaidi MR, Chen Y, Ma J-X, and Anderson RE (2004). Targeted expression of Cre recombinase to cone photoreceptors in transgenic mice. Mol. Vis 10, 1011–1018. [PubMed: 15635292]

Madisen L, Zwingman TA, Sunkin SM, Oh SW, Zariwala HA, Gu H, Ng LL, Palmiter RD, Hawrylycz MJ, Jones AR, et al. (2010). A robust and high-throughput Cre reporting and characterization system for the whole mouse brain. Nat. Neurosci 13, 133–140. [PubMed: 20023653]

Makous WL (1997). Fourier models and the loci of adaptation. J. Opt. Soc. Am. A Opt. Image Sci. Vis 14, 2323–2345. [PubMed: 9291604]

Marc RE, and Jones BW (2003). Retinal remodeling in inherited photoreceptor degenerations. Mol. Neurobiol 28, 139–147. [PubMed: 14576452]

Michalakis S, Schäferhoff K, Spiwoks-Becker I, Zabouri N, Koch S, Koch F, Bonin M, Biel M, and Haverkamp S (2013). Characterization of neurite outgrowth and ectopic synaptogenesis in response to photoreceptor dysfunction. Cell. Mol. Life Sci. 70, 1831–1847. [PubMed: 23269435]

Morgan JL, Schubert T, and Wong ROL (2008). Developmental patterning of glutamatergic synapses onto retinal ganglion cells. Neural Dev. 3, 8. [PubMed: 18366789]

Morgan JL, Soto F, Wong ROL, and Kerschensteiner D (2011). Development of cell type-specific connectivity patterns of converging excitatory axons in the retina. Neuron 71, 1014–1021. [PubMed: 21943599]

Naoi M, and Maruyama W (1999). Cell death of dopamine neurons in aging and Parkinson's disease. Mech. Ageing Dev 111, 175–188. [PubMed: 10656535]

Okawa H, Della Santina L, Schwartz GW, Rieke F, and Wong RO (2014). Interplay of cell-autonomous and nonautonomous mechanisms tailors synaptic connectivity of converging axons in vivo. Neuron 82, 125–137. [PubMed: 24698272]

Ratnam K, Carroll J, Porco TC, Duncan JL, and Roorda A (2013). Relationship between foveal cone structure and clinical measures of visual function in patients with inherited retinal degenerations. Invest. Ophthalmol. Vis. Sci 54, 5836–5847. [PubMed: 23908179]

Reiter HO, Waitzman DM, and Stryker MP (1986). Cortical activity blockade prevents ocular dominance plasticity in the kitten visual cortex. Exp. Brain Res 65, 182–188. [PubMed: 3803504]

Santina LD, and Ou Y (2018). Biolistic labeling of retinal ganglion cells. Methods Mol. Biol 1695, 161–170. [PubMed: 29190026]

Schwartz GW, Okawa H, Dunn FA, Morgan JL, Kerschensteiner D, Wong RO, and Rieke F (2012). The spatial structure of a nonlinear receptive field. Nat. Neurosci 15, 1572–1580. [PubMed: 23001060]

Sher A, Jones BW, Huie P, Paulus YM, Lavinsky D, Leung L-SS, Nomoto H, Beier C, Marc RE, and Palanker D (2013). Restoration of retinal structure and function after selective photocoagulation. J. Neurosci 33, 6800–6808. [PubMed: 23595739]

Smirnakis SM, Brewer AA, Schmid MC, Tolias AS, Schüz A, Augath M, Inhoffen W, Wandell BA, and Logothetis NK (2005). Lack of long-term cortical reorganization after macaque retinal lesions. Nature 435, 300–307. [PubMed: 15902248]

Sorensen SA, and Rubel EW (2006). The level and integrity of synaptic input regulates dendrite structure. J. Neurosci 26, 1539–1550. [PubMed: 16452677]

Soto F, Ma X, Cecil JL, Vo BQ, Culican SM, and Kerschensteiner D (2012). Spontaneous activity promotes synapse formation in a cell-type-dependent manner in the developing retina. J. Neurosci 32, 5426–5439. [PubMed: 22514306]

Strettoi E, Porciatti V, Falsini B, Pignatelli V, and Rossi C (2002). Morphological and functional abnormalities in the inner retina of the rd/rd mouse. J. Neurosci 22, 5492–5504. [PubMed: 12097501]

Strettoi E, Pignatelli V, Rossi C, Porciatti V, and Falsini B (2003). Remodeling of second-order neurons in the retina of rd/rd mutant mice. Vision Res. 43, 867–877. [PubMed: 12668056]

Sweeney LB, Chou Y-H, Wu Z, Joo W, Komiyama T, Potter CJ, Kolodkin AL, Garcia KC, and Luo L (2011). Secreted semaphorins from degenerating larval ORN axons direct adult projection neuron dendrite targeting. Neuron 72, 734–747. [PubMed: 22153371]

Tien N-W, Soto F, and Kerschensteiner D (2017). Homeostatic plasticity shapes cell-type-specific wiring in the retina. Neuron 94, 656–665.e4. [PubMed: 28457596]

Vessey KA, Greferath U, Aplin FP, Jobling AI, Phipps JA, Ho T, De Iongh RU, and Fletcher EL (2014). Adenosine triphosphate-induced photoreceptor death and retinal remodeling in rats. J. Comp. Neurol 522, 2928–2950. [PubMed: 24639102]

Villa KL, Berry KP, Subramanian J, Cha JW, Oh WC, Kwon H-B, Kubota Y, So PTC, and Nedivi E (2016). Inhibitory synapses are repeatedly assembled and removed at persistent sites in vivo. Neuron 89, 756–769. [PubMed: 26853302]

Wallace H, and Fox K (1999). The effect of vibrissa deprivation pattern on the form of plasticity induced in rat barrel cortex. Somatosens. Mot. Res 16, 122–138. [PubMed: 10449061]

Wallace H, Glazewski S, Liming K, and Fox K (2001). The role of cortical activity in experience-dependent potentiation and depression of sensory responses in rat barrel cortex. J. Neurosci 21, 3881–3894. [PubMed: 11356876]

Wandell BA, and Smirnakis SM (2009). Plasticity and stability of visual field maps in adult primary visual cortex. Nat. Rev. Neurosci 10, 873–884. [PubMed: 19904279]

Wang YV, Weick M, and Demb JB (2011). Spectral and temporal sensitivity of cone-mediated responses in mouse retinal ganglion cells. J. Neurosci 31, 7670–7681. [PubMed: 21613480]

Wässle H, Puller C, Müler F, and Haverkamp S (2009). Cone contacts, mosaics, and territories of bipolar cells in the mouse retina. J. Neurosci 29, 106–117. [PubMed: 19129389]

Wong ROL, and Ghosh A (2002). Activity-dependent regulation of dendritic growth and patterning. Nat. Rev. Neurosci 3, 803–812. [PubMed: 12360324]

Zayit-Soudry S, Duncan JL, Syed R, Menghini M, and Roorda AJ (2013). Cone structure imaged with adaptive optics scanning laser ophthalmoscopy in eyes with nonneovascular age-related macular degeneration. Invest. Ophthalmol. Vis. Sci 54, 7498–7509. [PubMed: 24135755]

Highlights

- Type 6 bipolar cell dendrites remodel following cone death in mature retina
- Bipolar cell input synapses are cone dependent, while output synapses are invariant
- Cone loss leads to narrower excitation and wider inhibition of $A_{ON\text{-}S}$ ganglion cells
- Spatial receptive field changes are not recapitulated by partial cone stimulation

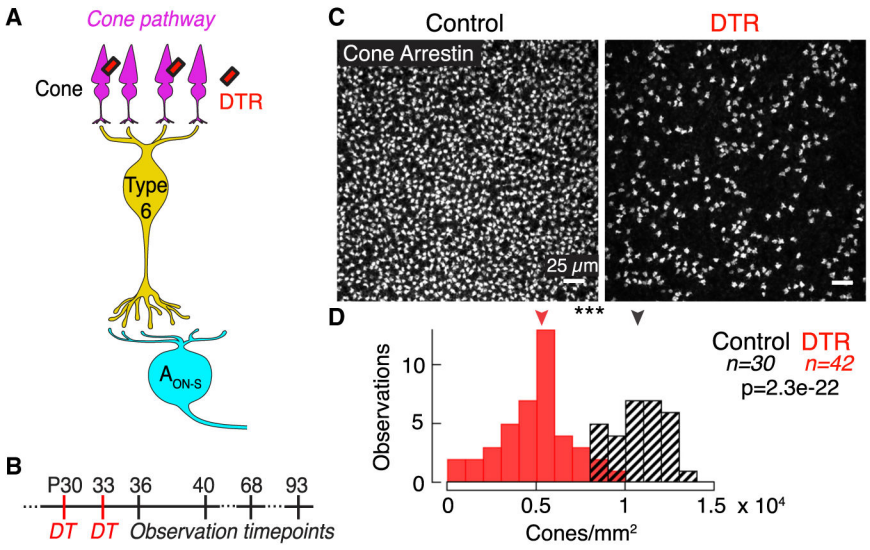

Figure 1. Diphtheria Toxin Receptor System Ablates Majority of Cones in the Mature Mouse Retina

(A) Schematic of the direct cone pathway: cones → type 6 ON cone bipolar cell → $A_{ON\text{-}S}$ ganglion cell. The diphtheria toxin receptor (DTR) is expressed in a subset of cones driven under either the promoter for short- or middle-wavelength opsin (see Figure S1).

(B) Timeline of experiments indicating DT injections and observation time points in post-natal (P) days. The time points were chosen to capture early responses to cone death before gross retinal remodeling previously observed at >3 months following photoreceptor loss (see Figure S2 and Table S1).

(C) Confocal images of the cone pedicles labeled by immunostaining for cone arrestin in control and DTR conditions in ventral retina.

(D) Histogram of cone densities in control and DTR conditions across all intervals between DT injection and quantification. Arrowheads indicate median of each population. Asterisks indicate significance (see Results).

See also Figures S1 and S2 and Table S1.

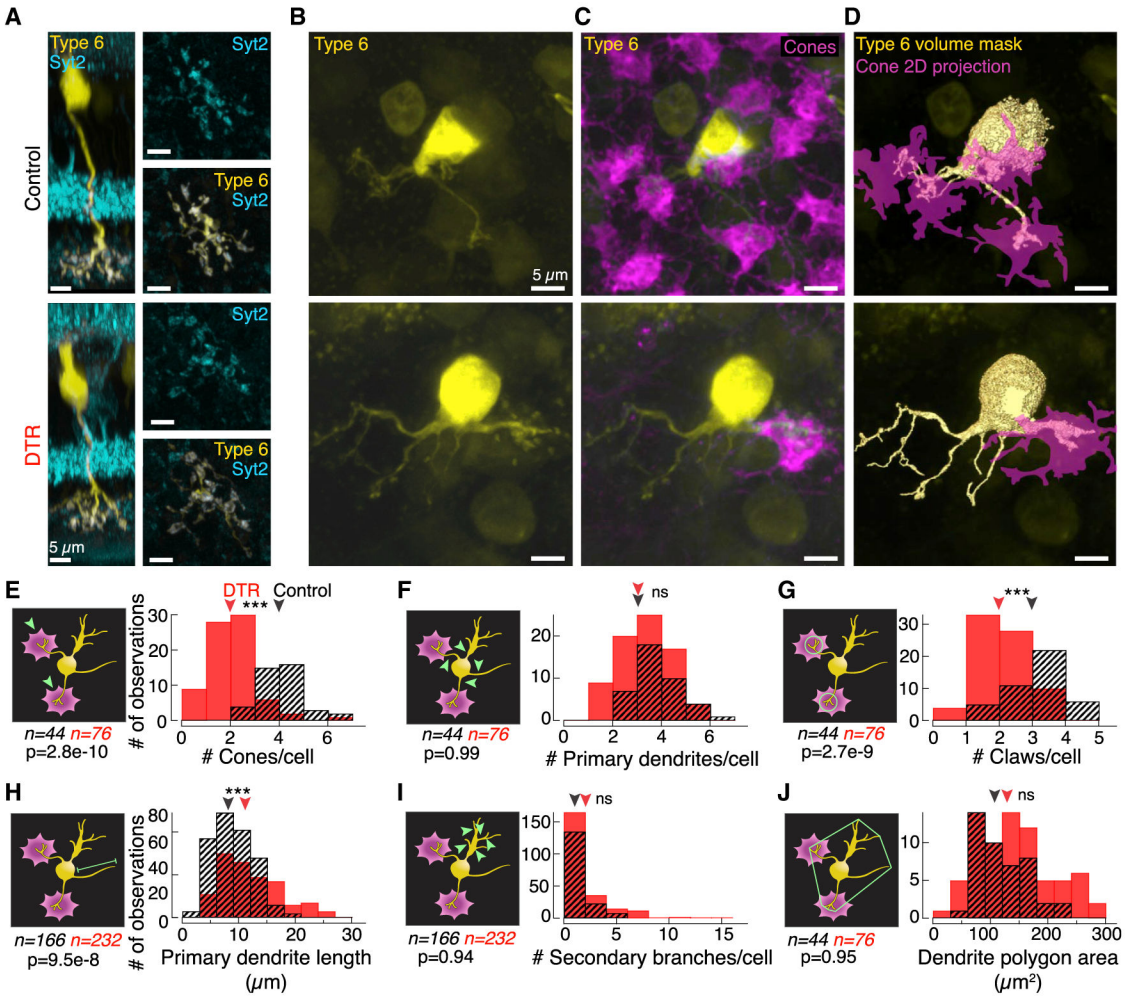

Figure 2. At the First-Order Synapse, Postsynaptic Type 6 Cone Bipolar Cell Dendrites Remodel after Cone Loss in Mature Retina

(A) Confocal images of type 6 cone bipolar cells labeled in the transgenic *Grm6-TdTomato* line. Side views of the isolated type 6 bipolar cells with Syt2 labeling of the type 2 and 6 bipolar cell axons. (Right) *En face* views of the bipolar cell axon terminal showing overlap with Syt2 within the axon in control (top) and DTR (bottom) retina.

(B and C) *En face* views of the type 6 cone bipolar cell (B) dendrites alone and (C) with cone pedicles labeled by cone arrestin in control (top) and DTR (bottom) retina.

(D) Rendered images of the type 6 bipolar cell dendrites (yellow) and associated cone pedicles (magenta). Such binary images of the bipolar cell dendrites and cones were used to determine volume overlap between the two structures.

(E–J) Histograms of (E) the number of cones that each type 6 bipolar cell contacts as determined by nonzero volume overlap between bipolar cell dendrites and cones; (F)the number of primary dendrites branching directly off the bipolar cell soma; (G)the number of claws per bipolar cell, defined by >3 secondary branches within a 10-μm-diameter circle; (H)the length of primary dendrites from the soma to the longest dendritic tip; (I) the number of second-order and greater branches coming from a primary branch that are not part of a claw structure; (J) the area of the polygon drawn around the vertices of the dendritic tips.

Arrowheads point to median. Asterisks indicate significance (see Results). Measurement examined is indicated on the schematic in green (left of each histogram). In the control condition, claws were seldom found without a cone contact. In the DTR condition, claws existed at terminals both with and without a cone contact. We cannot distinguish whether the claws in the absence of cones linger from previous cone contacts or are newly formed claws. Data combined across time points because there was no significant difference between shortest and longest time points (see Results). Number of samples (n) and p value for rank sum test noted in each panel.

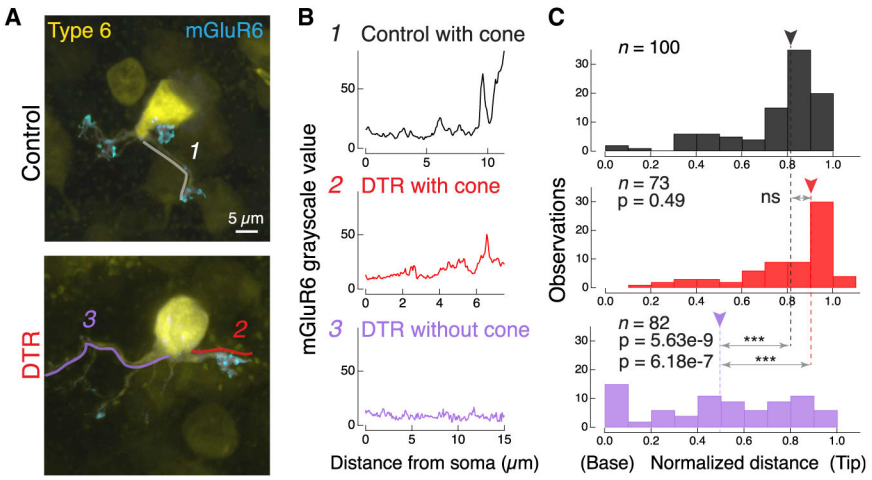

Figure 3. At the First-Order Synapse, Glutamate Receptor mGluR6 Is Regulated in a Cone-Dependent and Branch-Specific Manner after Cone Loss

(A) Confocal images of the type 6 bipolar cell dendrites labeled in the *Grm6-TdTomato* line (yellow) and the associated postsynaptic glutamate receptor mGluR6, labeled by immunostaining, within the dendrites (cyan). Same bipolar cells depicted in Figure 2D where cone locations are shown. Examples of line segments (1, 2, 3) traced from the soma to the dendritic tip. These line segments were used to quantify the grayscale value of mGluR6. Image of the mGluR6 within the bipolar cell has been adjusted to accentuate the location of synaptic puncta, but images analyzed for intensity values were not adjusted.

(B) Grayscale intensity value of mGluR6 channel for a (1) dendrite in control retina that contacts a cone, (2) dendrite in DTR retina that contacts a cone, and (3) dendrite in DTR retina that does not contact a cone.

(C) Histogram of peak location of mGluR6 from all line segments in control (black) and DTR bipolar cell dendrites, either ending with a cone (red) or without a cone (lavender). Number of dendrites within bins of mGluR6 peak location at the base next to the soma (0) to the tip (normalized to 1). Arrowheads point to the median. Horizontal arrows indicate comparisons made in each panel. Asterisks indicate significance (see Results). In control, only three line segments ended without a cone (data not shown). Data combined across time intervals. Number of dendritic line segments drawn for each condition (*n*).

See also Figure S3.

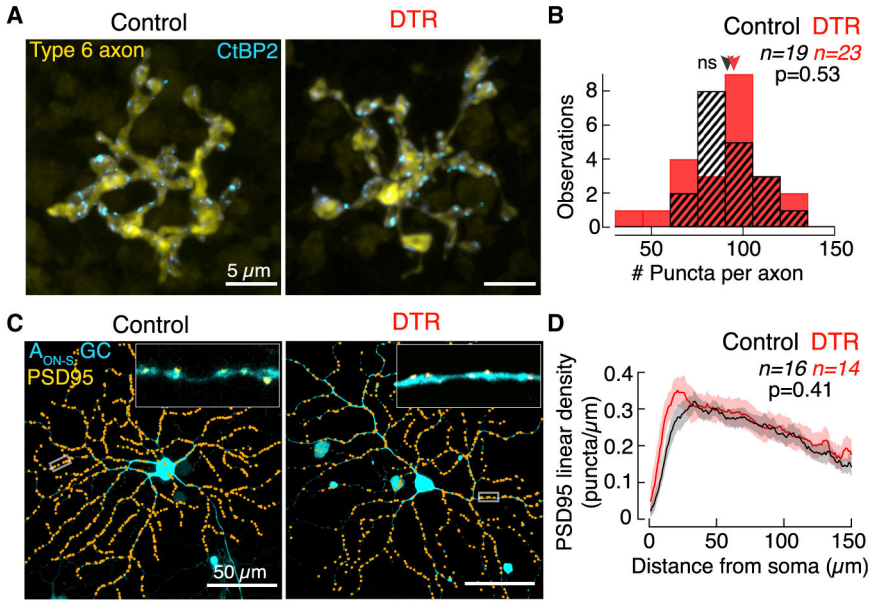

Figure 4. At the Second-Order Synapse, Type 6 Cone Bipolar Cell Glutamate Release Sites and $A_{ON\text{-}S}$ Ganglion Cell Postsynaptic Densities Are Stable after Cone Loss

(A) *En face* confocal images of type 6 cone bipolar cell axons labeled in the *Grm6-TdTomato* line (yellow). Glutamate release sites are labeled by immunostaining for CtBP2 (cyan). Only CtBP2 associated with the bipolar cell axon is shown.

(B) Histogram of the number of CtBP2 puncta within each type 6 cone bipolar cell axon terminal. Arrowheads point to median.

(C) *En face* images of the $A_{ON\text{-}S}$ ganglion cell labeled by a cell fill (cyan) and by postsynaptic density PSD95 fluorescent protein. The plasmids encoding these fluorescent proteins were introduced by gene gun. Upper right inset shows a stretch of dendrite with the raw PSD95 puncta (yellow) for the region outlined by the rectangle in the main image. Main image shows the identified locations of PSD95 (orange dots).

(D) Linear density of PSD95 puncta across dendritic distance from the soma to the periphery. Data represented as mean ± SEM.

See also Figure S4.

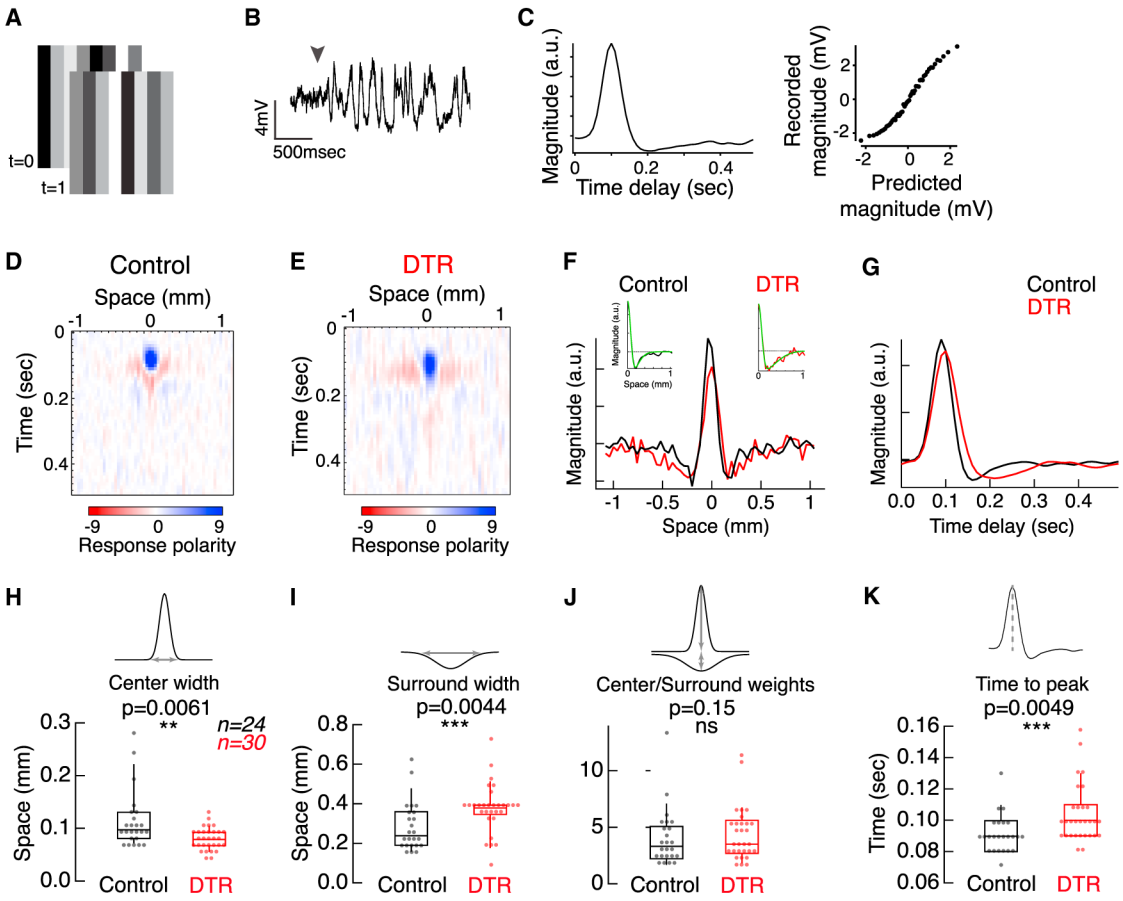

Figure 5. $A_{ON\text{-}S}$ Ganglion Cell Spatio-temporal Receptive Fields Widen Spatially and Slow Temporally after Cone Loss

(A) Example stimuli at two points in time where the intensity of each bar is randomly drawn from a Gaussian distribution.

(B) Voltage response of an $A_{ON\text{-}S}$ ganglion cell in current clamp. Arrowhead indicates the onset of the stimulus fluctuations on a mean background.

(C) One spatial slice of the temporal filter (left) and nonlinearity (right) calculated for a cell from control retina.

(D and E) Spatio-temporal receptive field obtained from a correlation of the response with the stimulus where red and blue represent opposite polarity responses for $A_{ON\text{-}S}$ ganglion cells recorded in control (D) and DTR (E) retina.

(F) Spatial receptive field for the cells shown in (D) and (E) taken for dominant principal components. (Inset) Difference of Gaussians fit (green) for each cell.

(G) Temporal filters from the first principal components of the cells from (D) and (E).

(H and I) Parameters of the difference of Gaussians fit show significantly narrower centers (H) and wider surrounds (I) for DTR receptive fields. Asterisks indicate significance (see Results). Boxplots show median with interquartile range (IQR) and whiskers from 10% to 90% of the data (see Figure S5).

(J) No significant difference was observed in the ratio of center and surround weights between control and DTR. Box plots show median with interquartile range and whiskers from 10% to 90% of the data.

(K) Time to peak of the temporal receptive fields for DTR cells are significantly slower than control cells. Box plots show median with interquartile range and whiskers from 10% to 90% of the data.

See also Figure S5.

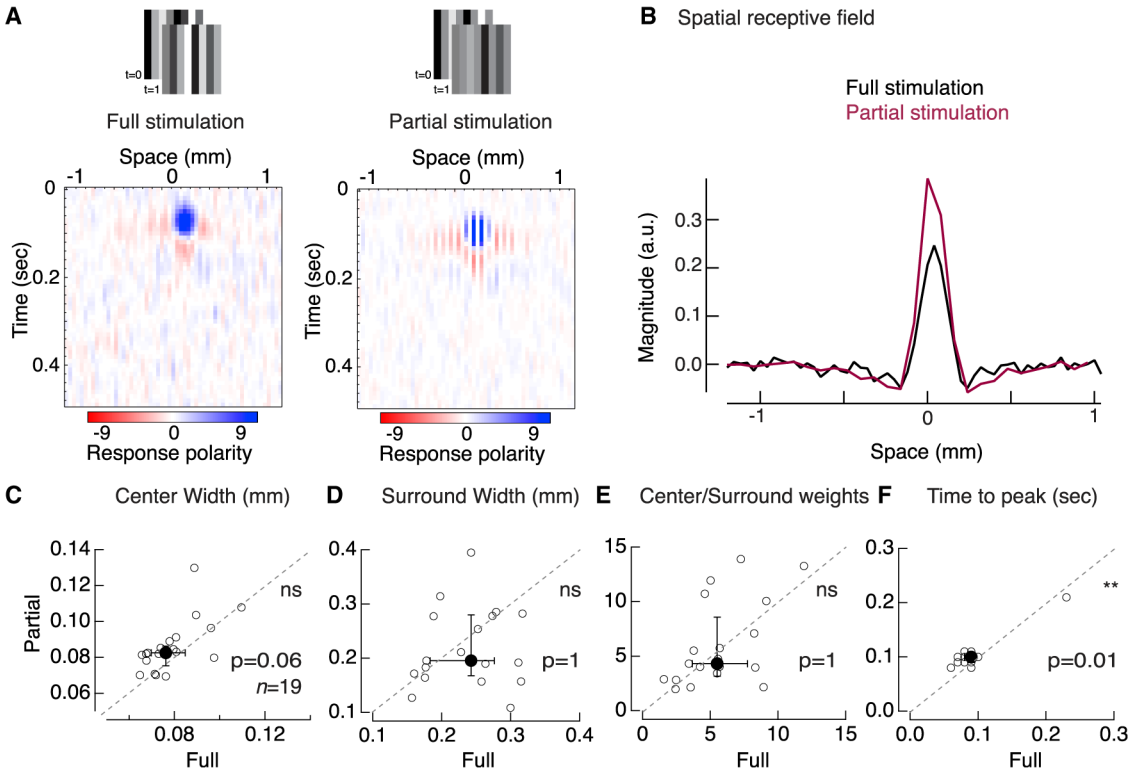

Figure 6. Control $A_{ON\text{-}S}$ Ganglion Cell Receptive Fields Retain Widths with Partial Stimulation

(A) Spatio-temporal receptive field obtained from voltage responses of a control $A_{ON\text{-}S}$ ganglion cell in current clamp. Receptive field obtained with a (left) full bar noise stimulus and (right) partial bar noise stimulus with every other bar held constant at the mean intensity. Receptive fields measured from the same cell. Red and blue represent opposite polarity responses.

(B) Spatial receptive field for the same $A_{ON\text{-}S}$ ganglion cell depicted in (A) either with full (black) or partial (maroon) stimulation.

(C–E) Gaussian fit parameters for receptive fields measured with full and partial stimulation within the same control $A_{ON\text{-}S}$ ganglion cells: (C) 1 SD center width, (D)1 SD surround width, and (E) center-to-surround weights. None of these parameters are significantly different between full and partial stimulation.

(F) Time to peak of temporal receptive fields. Individual cells (open circles) and median ± IQR (closed circles ± error bars). Dotted line represents line of slope unity. Slowing of the time to peak is the only parameter that partial stimulation of control retina mimics of the DTR condition (Figure 5).

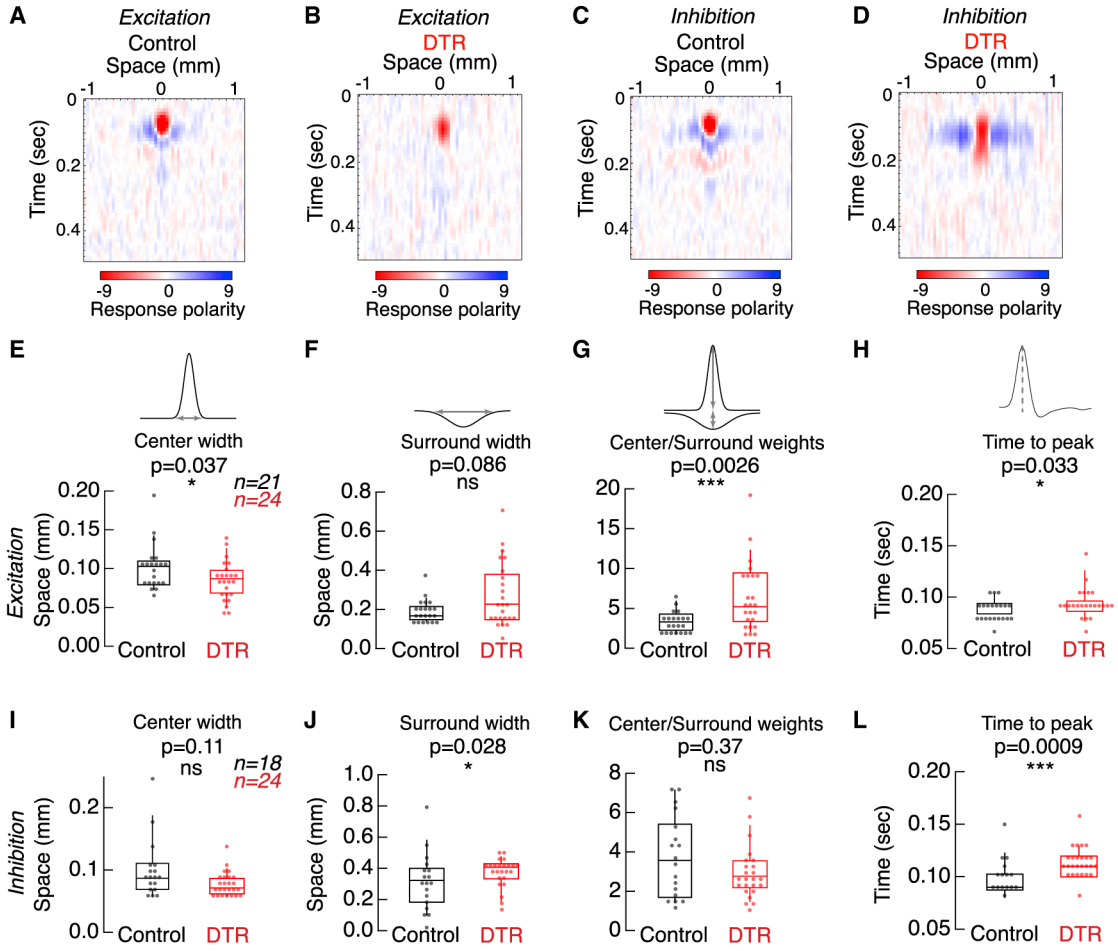

Figure 7. Excitation and Inhibition Drive Different Components of A_{ON-S} Ganglion Cell Receptive Field Changes after Cone Loss

(A and B) Spatio-temporal receptive field obtained from excitatory currents onto an A_{ON-S} ganglion cell recorded in voltage clamp at −60 mV in control (A) and DTR (B) retina.

(C and D) Spatio-temporal receptive field obtained from inhibitory currents onto an A_{ON-S} ganglion cell recorded in voltage clamp at +10 mV in control (C) and DTR (D)retina.

(E–G) Gaussian fit parameters for receptive fields measured from excitatory currents.

(E) Excitatory currents show significantly narrower centers after cone loss, although (F) show no change in surround widths after cone loss.

(G) The center-to-surround weights increase after cone loss.

(H) Time to peak of the temporal receptive fields is significantly slower.

(I–K) Gaussian fit parameters for receptive fields measured from inhibitory currents.

(I) Inhibitory currents show no change in center widths after cone loss, although (J) show significantly wider surrounds after cone loss.

(K) The center-to-surround weights are unchanged.

(L) Time to peak of the temporal receptive fields is significantly slower. Asterisks indicate significance (see Results).

(E–L) Boxplots show median with IQR and whiskers from 10% to 90% of the data.

KEY RESOURCES TABLE

REAGENT or RESOURCE	SOURCE	IDENTIFIER
Antibodies		
Rabbit polyclonal anti-calbindin	Swant	Cat# CB38; RRID: AB_2721225
Monoclonal mouse anti-CD68	Biorad	Cat# MCA1957; RRID: AB_322219
Goat anti-ChAT	Millipore	Cat# AB144P; RRID: AB_2079751
Rabbit polyclonal anti-cone arrestin	Millipore	Cat# AB15282; RRID:AB_1163387
Mouse monoclonal anti-CtBP2	BD Bioscience	Cat# 612044; RRID:AB_399431
Mouse monoclonal anti-GFAP	Biolegend	Cat# 835301; RRID: AB_2565344
Rabbit polyclonal anti-Iba1	Wako	Cat# 019-19741; RRID: AB_839504
Sheep polyclonal anti-mGluR6	Catherine Morgans, Kirill Martemyanov, Theodore Wensel	N/A
Mouse monoclonal anti-PKCalpha	Sigma-Aldrich	Cat# P5704; RRID:AB_477375
Rabbit anti-RBPMS	Phosphosolutions	Cat# 1830; RRID: AB_2492225
Mouse monoclonal anti-SMI-32	Stenberger Monoclonals	Cat# SMI-32P; RRID: AB_2314912
Rabbit anti-Sox9	Millipore	Cat#AB5535; RRID: AB_2239761
Mouse monoclonal anti-synaptotagmin II	Zebrafish International Resource Center	Cat# znp-1; RRID: AB_10013783
Mouse monoclonal anti-syntaxin1	Sigma-Aldrich	Cat# S0664; RRID: AB_477483
Mouse monoclonal anti-Trpm1-274	Melina Agosto and Theodore Wensel	N/A
Donkey polyclonal anti-rabbit-Alexa 488	Jackson Immunoresearch	Cat# 711-545-152; RRID:AB_2313584
Donkey polyclonal anti-sheep-Alexa 633	Molecular Probes	Cat# A21100; RRID:AB_10374307
Donkey polyclonal anti-mouse-Dylight 405	Jackson Immunoresearch	Cat# 715-475-150; RRID:AB_2340839
Donkey polyclonal anti-mouse-Alexa 647	Jackson Immunoresearch	Cat# 715-605-151; RRID:AB_2340863
Donkey polyclonal anti-sheep-Alexa 647	Jackson Immunoresearch	Cat# 713-605-147; RRID:AB_2340751
Donkey polyclonal anti-goat-Alexa 594	Jackson Immunoresearch	Cat# 705-585-147; RRID:AB_2340433
Donkey polyclonal anti-rabbit-Alexa 647	Jackson Immunoresearch	Cat# 711-605-152; RRID:AB_2492288
Rabbit polyclonal anti-red/green opsin	Millipore	Cat# AB5405; RRID:AB_177456
Goat polyclonal anti-OPN1SW	Santa Cruz Biotechnology	Cat# Sc-14363; RRID:AB_2158332
Chemicals, Peptides, and Recombinant Proteins		
Normal Donkey Serum	Jackson Immunoresearch	Cat# NC9624464
Ames Medium	United States Biological	Cat# A1372-25
Gold particles/microcarriers (1.6μm diameter)	Bio-Rad	Cat# 165-2264
Vectashield	Vector Laboratories	Cat# H-1000; RRID: AB_2336789
Experimental Models: Organisms/Strains		
Mouse model: *Grm6-tdTomato*	Kerschensteiner et al., 2009	N/A
Mouse model: *C57BL/6-Gt(ROSA)26Sortm1(HBEGF)Awai/J (DTR)*	The Jackson Laboratory	Cat# JAX:007900; RRID:IMSR_JAX:007900

REAGENT or RESOURCE	SOURCE	IDENTIFIER
Mouse model: *OPNSW1-Cre (BP-Cre)*	Akimoto et al., 2004	N/A
Mouse model: OPNMW1-Cre *(HRGP-Cre)*	Le et al., 2004	N/A
Mouse model: *hLMcone-GFP*	Fei and Hughes, 2001	N/A
Mouse *model:B6.Cg-Gt(ROSA)26Sortm6(CAG-ZsGreen1)Hze/J (Ai6)*	The Jackson Laboratory	Cat# JAX:007906; RRID:IMSR_JAX:007906
Recombinant DNA		
Plasmid: pCMV-CFP	Morgan et al., 2011	N/A
Plasmid: pCMV-PSD95-YFP	A.M. Craig, University of British Columbia (Morgan et al., 2008)	N/A
Software and Algorithms		
ImageJ	NIH	https://imagej.nih.gov/ij/, RRID: SCR_003070
Amira	Thermo-Fisher Scientific	https://www.thermofisher.com/us/en/home/industrial/electron-microscopy/electron-microscopy-instruments-workflow-solutions/3d-visualization-analysis-software/amira-life-sciences-biomedical.html, RRID: SCR_014305
Imaris	Bitplane	https://imaris.oxinst.com, RRID: SCR_007370
MATLAB	Mathworks	https://www.mathworks.com/products/matlab.html,RRID: SCR_001622
Igor Pro	Igor Pro	RRID:SCR_000325
Object Finder	Della Santina et al., 2013	https://lucadellasantina.github.io/ObjectFinder/
Symphony and Stage	Mark Cafaro and Fred Rieke	https://github.com/Symphony-DAS/symphony-v1/wiki https://github.com/Stage-VSS/stage-v1